JOURNAL OF COMPUTATIONAL PHYSICS **137,** 366–405 (1997)
ARTICLE NO. CP975805

Multiphase Dynamics in Arbitrary Geometries on Fixed Cartesian Grids

H. S. Udaykumar, Heng-Chuan Kan, Wei Shyy, and Roger Tran-Son-Tay

Department of Aerospace Engineering, Mechanics and Engineering Science
University of Florida, Gainesville, Florida 32611
E-mail: ush@confucius.aero.ufl.edu

Received July 31, 1996; revised July 21, 1997

In this work, a mixed Eulerian–Lagrangian algorithm, called *ELAFINT* (Eulerian Lagrangian algorithm for interface tracking) is developed further and applied to compute flows with solid–fluid and fluid–fluid interfaces. The method is capable of handling fluid flows in the presence of both irregularly shaped solid boundaries and moving boundaries on a fixed Cartesian grid. The field equations are solved on the underlying fixed grid using a collocated variable, pressure-based formulation. The moving boundary is tracked explicitly by the Lagrangian translation of marker particles. The moving boundary passes through the grid and the immersed boundary technique is used to handle its interaction with the underlying grid. The internal solid boundaries are dealt with by using a cut-cell technique. Particular attention is directed toward conservation and consistency in the vicinity of both phase boundaries. The complex geometry feature has been tested for a variety of flow problems. The performance of the immersed boundary representation is demonstrated in the simulation of Newtonian liquid drops. The combination of the two features is then employed in the simulation of motion of drops through constricted tubes. The capabilities developed here can be useful for solving flow problems involving moving and stationary complex boundaries.

1. INTRODUCTION

The challenges posed by fluid flow problems involving moving boundaries have resulted in a variety of computational techniques directed toward their solution (Shyy *et al.* [1]). The moving boundaries may represent material discontinuities in the flowfield, and their dynamics is coupled with that of the flow. Numerical methods

0021-9991/97 $25.00

applied to such problems are required to follow the evolution of the complex shapes often assumed by the moving boundaries. To tackle these evolving interfaces, as a natural extension of adaptive grid methods for stationary complex geometries, algorithms based on body-fitted coordinates have been applied to moving boundary problems (Kang and Leal [2], Glimm *et al.* [3]). A boundary-conforming grid arrangement is convenient and accurate; the discontinuity is always maintained and interfacial conditions are applied at the exact locations without any smearing or redistribution. However, when the interface deformation becomes large, it is difficult to adequately resolve the geometrical complexities while maintaining desired mesh control. Mesh skewness and stretching may impact negatively on accuracy and efficiency of the flow solver. The boundary-fitted grid method presents further difficulties when interfaces merge or fragment.

In simulating multiphase phenomena involving highly deformed interface shapes, purely Eulerian methods (Osher and Sethian [4], Kothe and Mjolsness [5], Sussman *et al.* [6], Chang *et al.* [44], Hou *et al.* [45]) have come to be widely used. In such methods, a fixed Cartesian grid is usually used, so problems associated with grid generation are circumvented. Eulerian methods based on the volume of fluid (Hirt and Nichols [7]) or level-set (Osher and Sethian [4], Sethian [8], Chang *et al.* [44], Hou *et al.* [45]) are popular methods to handle free-surface flows, such as wave-breaking, sloshing, and splashing type problems. In purely Eulerian methods, the details of the interface shape are not explicitly available, since the interface is deduced based on a computed field variable. The interface information needs to be obtained from an appropriate computed field variable in order to describe the details of the interface shape and curvature. An accurate estimation of the interface curvature is very important when capillarity plays a significant role in the interfacial physics. In tracking highly distorted interfaces with good accuracy, a combination of the strengths of Eulerian and Lagrangian methods has been shown to be useful. This mixed Eulerian–Lagrangian approach has been used in recent years for problems involving fluid–fluid (Unverdi and Tryggvason [9], Nobari *et al.* [10]) as well as solid–liquid interactions (Shyy *et al.* [1], Udaykumar and Shyy [11], Udaykumar *et al.* [12], Juric and Tryggvason [13]). These methods employ fixed structured grids and afford simplicity and availability of well-tested flow solvers. The only moving component is the interface which is a lower-dimensional surface overlying the fixed grid and is explicitly tracked.

One limitation of the methods based on fixed grids is that since they have traditionally employed Cartesian grids, complex flow geometries are difficult to incorporate. A complex geometry facility would be useful in studying the interaction of the moving boundary with flows in arbitrary domains. The representation of a solid boundary on a fixed Cartesian grid layout calls for special treatment, since the control volumes through which the irregular boundary passes become fragmented into solid and liquid regions. This situation is illustrated in Fig. 1. Quirk [14] detailed some of the procedures involved in dealing with cell fragments or cut cells in the framework of compressible, inviscid flows around stationary obstacles. However, the calculation of fluxes is not presented in detail in that work. Also in connection with compressible, inviscid flows, Pember *et al.* [15] use local refinement and a redistribution procedure to enforce conservation in the vicinity of the solid–fluid

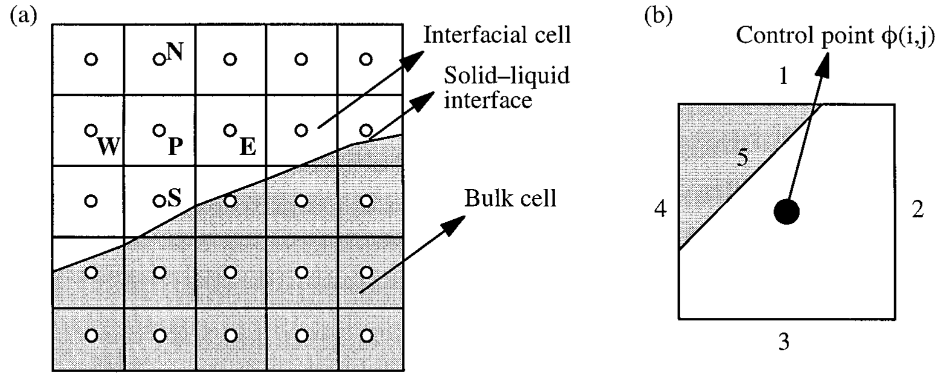

FIG. 1. Illustrations of (a) the situation when a solid object is represented on a Cartesian grid, (b) a typical control volume encountered in the vicinity of the solid–liquid interface (interfacial cell).

boundary. Arbitrary-shaped boundaries running through a Cartesian mesh have also been dealt with using finite element methods by Young *et al.* [16]. In Zeeuw and Powell [17] and Bayyuk *et al.* [18], a Cartesian grid is employed to track the motion of solid objects through an inviscid compressible fluid. Goldstein *et al.* [19, 20] have employed a modified immersed boundary technique (Peskin [21]) to impose no-slip boundary conditions over arbitrary-shaped solid boundaries. This facility has been found useful in going beyond simple geometries, an important consideration for the spectral methods in use therein. Turbulent flows around solid obstacles have been calculated using this approach and the results have been shown to compare favorably with experiment. The method, as used in these works, treats the solid boundary as a series of steps conforming with the Cartesian grid layout, i.e., in piecewise constant fashion. In contrast, a piecewise linear representation of the free surface was used by Miyata [22] for the simulation of wave breaking; the calculations were performed on a Cartesian grid using a finite difference technique. In a finite volume setting, Udaykumar and Shyy [23] used a cut-cell technique to compute incompressible, viscous flows in arbitrary geometries. In that work, it was demonstrated that by means of a suitably defined consistent mosaic of control volumes, it is possible to obtain accurate solutions for flows on Cartesian meshes. However, the staggered variable layout in Udaykumar and Shyy [23] rendered the measures adopted to handle the internal boundaries rather tedious. Here, we present a fixed grid methodology for the simulation of flow through complex geometries with moving two-fluid boundaries, simplified considerably by the choice of a collocated variable layout (Lien and Leschziner [24]). The performance of the flow solver in terms of stability and accuracy was thoroughly tested for various flow conditions. Results of our flow computations are presented in Section 3.

2. A MIXED EULERIAN–LAGRANGIAN SOLUTION ALGORITHM

2.1. Outline of the *ELAFINT* Algorithm

There are two distinct aspects to the computational framework, called *ELAFINT,* reported in Udaykumar *et al.* [12]. These are:

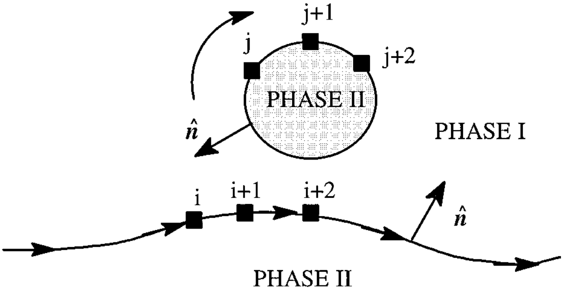

FIG. 2. Illustration of objects, markers, and normal convention in the description of interfaces.

(1) A pressure-based flow solver to simulate the incompressible fluid flow over a wide range of Reynolds numbers.

(2) A procedure to deal with the interaction of fixed arbitrary geometries and evolving moving boundaries with the flow.

The first aspect is straightforward and approached in a conventional manner using the robust pressure-based solution procedure detailed by Patankar [25] and in the context of more modern developments by Shyy [26]. The scheme to track the moving fronts and describe complex geometries is summarized below, following which the flow solver and its interaction with the internal boundaries is described.

2.1.1. *Interface Tracking Algorithm*

The interfaces are described by means of markers indexed sequentially and separated into objects. There is no restriction on the number of objects or on the end conditions that can be imposed on these curves. As shown in Fig. 2, the objects can be open or closed. Furthermore, they can be fixed or moving. They can enclose different phases or materials with different properties. Once the interface description is obtained in terms of markers and their positions, the shape characteristics such as normals and curvatures can be extracted. The convention adopted by the algorithm is to consider the normal to the interface as pointing from phase II to phase I, as shown in Fig. 2, such that when one traverses the interface along the marker sequence, phase II lies to the right. In order to handle multiple-valued interfaces, the interface tracking algorithm employs piecewise polynomial fits to compute the necessary shape derivatives at each marker location. Facility exists to construct quadratic or cubic-spline functions $x_i(s)$ and $y_i(s)$. The polynomial fits are obtained by parametrizing the curve as a function of arclength s so that, for the ith marker,

$$x_i = x_i(s), \quad y_i = y_i(s). \tag{1}$$

Then the normal and curvature are obtained by taking appropriate derivatives of these piecewise polynomials. Thus, the components of the normal are

$$n_x = \frac{y_s}{(x_s^2 + y_s^2)^{1/2}}, \quad n_y = -\frac{x_s}{(x_s^2 + y_s^2)^{1/2}}. \tag{2}$$

The curvature κ is, for the two-dimensional case,

$$\kappa = \nabla \cdot \hat{\boldsymbol{n}} = \frac{y_s x_{ss} - y_{ss} x_s}{(y_s^2 + x_s^2)^{3/2}}, \tag{3}$$

and the axisymmetric case,

$$\kappa = \frac{x_s}{y(y_s^2 + x_s^2)^{3/2}} + \frac{y_s x_{ss} - y_{ss} x_s}{(y_s^2 + x_s^2)^{3/2}}. \tag{4}$$

Interfacial markers are advected to their new positions by Lagrangian translation. Thus,

$$x_l^{k+1} = x_l^k + \Delta t \, u_l \tag{5}$$

$$y_l^{k+1} = y_l^k + \Delta t \, v_l, \tag{6}$$

where subscript l indicates the interfacial marker number and superscript k implies the time level. It was demonstrated (Shyy *et al.* [1], Udaykumar and Shyy [11, 23]) that the interface tracking procedure can handle extreme deformation, including topological changes such as repeated mergers and breakups. It was also established that the interface tracking facility is versatile and accurate.

Once the objects are described on the computational domain, the interaction with the flowfield needs to be established. This is mainly done by providing the following information:

(1) The cell in which each interface marker lies.

(2) The markers contained within each interfacial cell (i.e., control volume through which the interface passes).

Since a Cartesian grid is employed, establishing these relationships is a straightforward task. Armed with this information, one can provide and extract information of use to the flow solver and interface tracking components of the algorithm. Based on the information mentioned above, the flow solver can incorporate either changes in the control volume definitions (as in the cut-cell approach) or appropriate source term contributions (as in the immersed boundary technique). These two approaches enable the effects of the internal stationary, as well as moving boundaries, to be communicated to the flowfield. In turn, based on the flowfield developed, the motion of the interface can be determined. In Udaykumar and Shyy [11], moving as well as stationary solid–liquid boundaries were handled by the cut-cell technique. In this work, the cut-cell technique is retained for the stationary solid–liquid boundaries, while the immersed boundary technique (Peskin [21], Fauci and Peskin [27], Unverdi and Tryggvason [9]) is used to treat moving two-fluid boundaries. These issues are discussed in the following sections.

2.2. Formulation

Consider the two-dimensional planar or axisymmetric, incompressible Navier–Stokes flow. The governing equations in conservation forms are:

Continuity equation

$$\frac{\partial \varrho}{\partial t} + \frac{\partial}{\partial x}(\varrho u) + \frac{1}{y^m}\frac{\partial}{\partial y}(y^m \varrho v) = 0; \tag{7}$$

Momentum equations,

$$\begin{aligned}
&\frac{\partial(\varrho u)}{\partial t} + \frac{\partial}{\partial x}(\varrho u u) + \frac{1}{y^m}\frac{\partial}{\partial y}(y^m \varrho v u) \\
&\qquad = -\frac{\partial p}{\partial x} + \frac{\partial}{\partial x}\left(\mu \frac{\partial u}{\partial x}\right) + \frac{1}{y^m}\frac{\partial}{\partial y}\left(y^m \mu \frac{\partial u}{\partial y}\right) + S_u, &(8)\\
&\frac{\partial(\varrho v)}{\partial t} + \frac{\partial}{\partial x}(\varrho u v) + \frac{1}{y^m}\frac{\partial}{\partial y}(y^m \varrho v v) \\
&\qquad = -\frac{\partial p}{\partial y} - \mu\frac{m v}{y^2} + \frac{\partial}{\partial x}\left(\mu \frac{\partial v}{\partial x}\right) + \frac{1}{y^m}\frac{\partial}{\partial y}\left(y^m \mu \frac{\partial v}{\partial y}\right) + S_v; &(9)
\end{aligned}$$

Energy equation,

$$\frac{\partial(\varrho T)}{\partial t} + \frac{\partial}{\partial x}(\varrho u T) + \frac{1}{y^m}\frac{\partial}{\partial y}(y^m \varrho v T) = \frac{\partial}{\partial x}\left(\mu \frac{\partial T}{\partial x}\right) + \frac{1}{y^m}\frac{\partial}{\partial y}\left(y^m \mu \frac{\partial T}{\partial y}\right), \tag{10}$$

where $m = 0$ for the planar case and 1 for the axisymmetric case. In the above, ϱ is the fluid density, u and v are the fluid velocity components, T is temperature, p is pressure, and μ is the coefficient of viscosity. S_u and S_v represent the source terms in x- and y-momentum equations which include, for example, the buoyancy term under the Boussinesq approximation and the surface tension contributions discussed later.

The boundary conditions to be applied on the interface for cases involving no mass exchange across it are the continuity condition and normal stress balance,

$$(V_n)_1 = (V_n)_2 = (V_n)_I \tag{11}$$

$$p_2 - p_1 = \gamma\kappa + \mu_2\left(\frac{\partial V_n}{\partial n}\right)_2 - \mu_1\left(\frac{\partial V_n}{\partial n}\right)_1, \tag{12}$$

where subscripts 1 and 2 represent the two adjoining fluids and I represents the interface, γ is the surface tension, V_n is the normal velocity component, and κ is

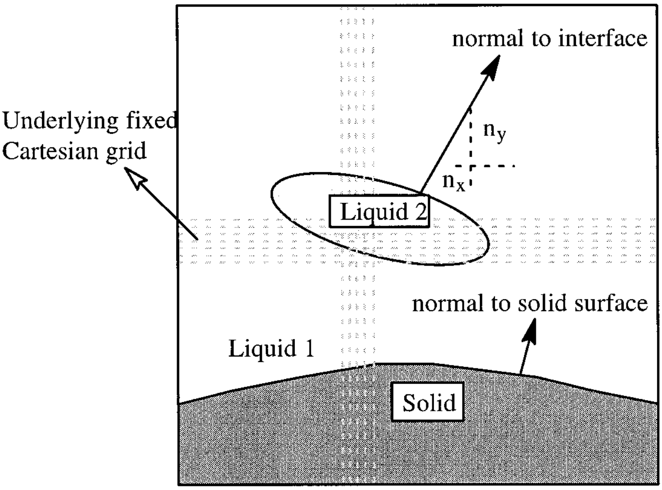

FIG. 3. Illustration of the interaction of the solid–liquid and liquid–liquid boundaries with Cartesian grid. The solid–liquid is treated using cut-cell technique, while the liquid–liquid interface is modeled with the immersed boundary technique.

the surface curvature, with the normal pointing from fluid 2 into fluid 1, as shown in Fig. 3.

2.3. Discretization Procedure of Flow Equations

The discretization of the governing equations is carried out using a control volume formulation, and will be presented here with particular reference to two-dimensional planar flow. Similar treatment applies for the axisymmetric case. Consider the conservation law for the transport variable ϕ, defined to be (a) 1 for the continuity equation, (b) u and v for the x- and y-momentum equations, and (c) *specific enthalpy* ($h = C_p T$) for the energy equation. In the general case, we have

$$\frac{\partial(\varrho\phi)}{\partial t} + \nabla \cdot (\varrho \mathbf{u} \phi) = (\nabla \cdot \Gamma \nabla \phi) + S. \tag{13}$$

The control volumes in the vicinity of a solid boundary passing through the grid are irregularly shaped and in the general case can assume a five-sided shape as shown in Fig. 1b. In order to evaluate the fluxes through the cell faces, we integrate Eq. (13) over the control volume and employ the divergence theorem for two-dimensional problems to obtain

$$\int_A \frac{\partial \varrho\phi}{\partial t} dA + \oint_l (\varrho \mathbf{u} \phi) \cdot \mathbf{n} dl = \oint_l (\Gamma \nabla \phi) \cdot \mathbf{n} dl + \int_A S dA, \tag{14}$$

where the second term on the left-hand side is now the line integral of the outward normal convective fluxes and the first term on the right side is the line integral of the outward normal diffusion fluxes through the faces of the control volume.

We now proceed to discretize each of the terms in Eq. (14) for the control volume shown. Thus

$$\int_A \frac{\partial \varrho \phi}{\partial t} dA = \frac{\varrho_{i,j}^{k+1}\phi_{i,j}^{k+1} - \varrho_{i,j}^{k}\phi_{i,j}^{k}}{\delta t} A_{cv}\,, \tag{15}$$

where the superscript k, $k+1$ indicate the time levels and δt is the time step size. A_{cv} is the area of the irregular control volume. The time derivative is discretized in the backward Euler form leading to an implicit-in-time solution procedure which relaxes the time step constraints in comparison with explicit schemes. Next,

$$\oint_l (\varrho \mathbf{u} \phi) \cdot \mathbf{n} dl = \sum_{l=1}^{5} (\varrho_l u_l \phi_l)^{k+1}\, dl_l \tag{16}$$

is the summation of the convective normal effluxes through each cell face of the control volume shown in Fig. 1b. The superscript $k+1$ indicates the implicit nature of the scheme. Following Shyy *et al.* [1] and Udaykumar *et al.* [12], the diffusion fluxes are computed as

$$\oint_l (\Gamma \nabla \phi) \cdot \mathbf{n} dl = \sum_{l=1}^{5} \left(\Gamma_l \left(\frac{\partial \phi}{\partial n} \right)_l \right)^{k+1} dl_l\,, \tag{17}$$

where n denotes the normal direction. Let us denote the source term as

$$\int_A S dA = \overline{S}. \tag{18}$$

Here $\overline{S}$ contains contributions from the pressure and body force terms. Substituting the above Eqs. (15–18) in Eq. (14) one obtains the discretized form as

$$\frac{\varrho_{i,j}^{k+1}\phi_{i,j}^{k+1} - \varrho_{i,j}^{k}\phi_{i,j}^{k}}{\delta t} A_{cv} + \sum_{l=1}^{5} (\varrho_l u_l \phi_l)^{k+1}\, dl_l = \sum_{l=1}^{5} \left(\Gamma_l \left(\frac{\partial \phi}{\partial n} \right)_l \right)^{k+1} dl_l + \overline{S}. \tag{19}$$

In particular the discrete form of the continuity equation can be written as

$$\frac{(\varrho_{i,j}^{k+1} - \varrho_{i,j}^{k})}{\delta t} A_{cv} + \sum_{l=1}^{5} (\varrho_l u_l)^{k+1}\, dl_l = 0. \tag{20}$$

Now multiplying Eq. (20) by the value $\phi_{i,j}^{k}$ and subtracting from Eq. (19) gives

$$\frac{\varrho_{i,j}^{k}(\phi_{i,j}^{k+1} - \phi_{i,j}^{k})}{\delta t} A_{cv} + \sum_{l=1}^{5} (\varrho_l u_l (\phi_l - \phi_{i,j}))^{k+1}\, dl_l = \sum_{l=1}^{5} \left(\Gamma_l \left(\frac{\partial \phi}{\partial n} \right)_l \right)^{k+1} dl_l + \overline{S}. \tag{21}$$

In the notation of the pressure-based methodology (Patankar [25], Shyy [26]), we cast the final discretized form as

$$a_P \phi_P = a_N \phi_N + a_S \phi_S + a_E \phi_E + a_W \phi_W + b, \tag{22}$$

where the subscripts refer to the points in the five-point stencil, shown in Fig. 1a for a typical bulk cell. The last term on the right, b, contains the discretized contributions from the source terms and boundary conditions and is given by

$$b = \overline{S} + \Gamma_I \left(\frac{\partial \phi}{\partial n_I}\right) dl_I - \varrho_I u_{nI} dl_I (\phi_I - \phi_P). \tag{23}$$

The form of the coefficients $a_{P,E,W,N,S}$ depends on the convection scheme employed. In this work, we employ the second-order central difference scheme for the convection term. Diffusion and pressure terms are also discretized using central differences. When cast in the matrix form Eq. (22) reads

$$[C]\,[\Phi] = [B], \tag{24}$$

where $[C]$ is a pentadiagonal coefficient matrix, Φ is the solution vector, and B is a source vector. The procedure usually adopted is to solve the system of equations in iterative fashion employing a line SOR method which calls for a tridiagonal matrix solution procedure. A pressure-correction procedure provides the pressure field consistent with mass conservation. In the pressure-based methodology, it is common practice to use a staggered layout of variables. However, here we use a collocated arrangement of the dependent variables. This calls for special measures, called momentum interpolation (Rhie and Chow [28], Lien and Leschziner [24]), when estimating cell face velocities. The details of momentum interpolation will be discussed next.

2.3.1. *Momentum Interpolation*

One of the key issues in using a pressure-based solver is the grid arrangement. The staggered grid layout has been preferred for incompressible flow computations for many decades due to its many advantages (Patankar [25], Shyy [26]). However, the collocated arrangement has desirable attributes in terms of simplicity and economy and has come into more common use. For example, in the present case, in dealing with the internal boundaries, whether by the cut-cell or the immersed boundary technique, the use of a collocated variable layout leads to the treatment of a single set of control volumes for all the dependent variables (namely, u, v, p, and T). In the case of a staggered system, three sets of control volumes, for u, v and the scalars need to be considered and the data structures associated with the cut-cell, as well as the immersed boundary technique, need to be computed and stored. A particular instance is the identification of the phase of the control volume. When the staggered layout is used the phase in which the control points for the u, v and scalar variables lie needs to be determined separately, while in the collocated layout only one set of control volumes needs to be handled. This leads to a considerable savings both in terms of the programming effort and in the computational effort expended in obtaining the information regarding the interaction of interfaces with the flowfield.

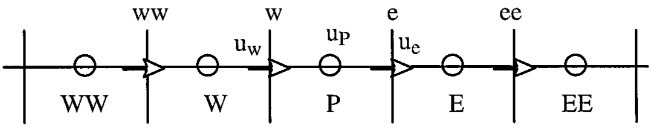

FIG. 4. Schematic of 1D collocated grid layout.

One potential difficulty of the collocated grid is the occurrence of spurious oscillations in the pressure and velocity fields, leading to numerical instabilities for certain flow problems (Patankar [25]). This is due to the fact that the collocated grid arrangement leads to decoupling of pressure and velocity fields when the central difference operator is employed in discretizing gradients in the flowfield. However, with the incorporation of momentum interpolation, introduced by Rhie and Chow [28], it is possible to prevent the onset of checkerboard phenomena resulting from decoupling between pressure and velocity fields. However, as pointed out by Majumdar [29], the momentum interpolation form proposed by Rhie and Chow [28] can lead to solutions that depend on the relaxation factor employed in the iterative solution procedure. Lien and Leschziner [24] have presented a form of momentum interpolation that overcomes this problem and have applied this measure to obtain solutions for a wide range of flow problems, including unsteady, turbulent, and shocked flows. In our implementation, we use the version of momentum interpolation, recommended by Lien and Leschziner [24], to evaluate the velocities at the faces of the control volume.

Essentially, momentum interpolation introduces a third-order dissipation in estimating the cell face velocity. This can be seen as follows. The discretized momentum equations for the u-velocity control points shown in Fig. 4, u_P and u_E, based on Eq. (22) are given in the one-dimensional case by

$$a_P u_P = \sum_{nb=E,W} a_{nb} u_{nb} + b_u - (p_e - p_w)_P \tag{25}$$

$$a_E u_E = \sum_{nb=EE,P} a_{nb} u_{nb} + b_u - (p_e - p_w)_E \,, \tag{26}$$

where subscript nb implies neighboring points in the stencil, b_u here represents the source term not including the pressure term, with $a_P = \sum_{nb=E,W} a_{nb}$ and $a_E = \sum_{nb=EE,P} a_{nb}$. The relative positions of the points subscripted, P, E, W, EE, and WW, are shown in Fig. 4.

Equation (25) and Eq. (26) can be written as

$$u_P = \frac{H_P}{a_P} - \frac{1}{a_P}(p_e - p_w)_P \tag{27}$$

$$u_E = \frac{H_E}{a_E} - \frac{1}{a_E}(p_e - p_w)_E, \tag{28}$$

where $H_p = \sum_{nb=E,W} a_{nb} u_{nb} + b_u$ and $H_E = \sum_{nb=EE,P} a_{nb} u_{nb} + b_u$. In performing the interpolation, it is assumed that

$$\frac{H_e}{a_e} = \frac{1}{2}\left(\frac{H_P}{a_P} + \frac{H_E}{a_E}\right). \tag{29}$$

Then, substituting Eq. (27) and Eq. (28) into Eq. (29), the interpolation for the face velocity u_e can be expressed as

$$u_e = \frac{1}{2}\left[u_P - \frac{1}{a_P}(p_w - p_e)_P + u_E - \frac{1}{a_E}(p_w - p_e)_E\right] + \frac{1}{a_e}(p_P - p_E), \tag{30}$$

or alternatively,

$$u_e = \frac{1}{2}(u_P + u_E) + \Bigg\{\underbrace{\frac{1}{a_e}(p_P - p_E)}_{\text{Ⓘ}} - \underbrace{\frac{1}{2}\left[\frac{1}{a_P}(p_w - p_e)_P + \frac{1}{a_E}(p_w - p_e)_E\right]}_{\text{Ⓘ Ⓘ}}\Bigg\}. \tag{31}$$

In Eq. (31) the face velocity of the control volume is directly linked to the two adjacent cell-center pressures through the term I above. This ensures that strong coupling between the pressure and velocity fields is retained. The second term, indicated as II, is the pressure smoothing term, which eliminates the nonphysical wavy pressure or velocity fields. In fact, it can be shown that Eq. (31) can be recast, following some manipulation (Lien and Leschziner [24]), as

$$u_e = \frac{1}{2}(u_P + u_E) + \left(\frac{\partial^3 p}{\partial x^3}\right)\mathcal{O}(\Delta x^3). \tag{32}$$

This brings to light the fact that momentum interpolation adds a third-order dissipation term to the cell face velocity, relative to straightforward averaging of adjacent cell-center velocities. Thus, spurious pressure oscillations are eliminated. Typically, iterative procedures are used to solve the discretized momentum equations, and underrelaxation can be implemented in Eq. (25) in the form

$$u_P^{**} = \alpha\, u_P + (1 - \alpha)\, u_P^{*}, \tag{33}$$

where α is the underrelaxation factor, u_P is the current iteration value, u_P^* is the value of u_P at the previous iteration, while u_P^{**} is the value obtained after relaxation. Similarly,

$$u_E^{**} = \alpha\, u_E + (1 - \alpha)\, u_E^{*}. \tag{34}$$

Therefore, the cell face velocity, after including the relaxation factor, is

$$\begin{aligned} u_e^{**} &= \alpha\, u_e + (1 - \alpha)\, u_e^{*} \\ &= \alpha\left\{\frac{1}{2}(u_P + u_E) + \frac{1}{a_e}(p_P - p_E) - \frac{1}{2}\left[\frac{1}{a_P}(p_w - p_e)_P + \frac{1}{a_E}(p_w - p_e)_E\right]\right\} \\ &\quad + (1 - \alpha)\, u_e^{*}. \end{aligned} \tag{35}$$

The momentum interpolation as obtained from Eq. (35) yields flowfields independent of the relaxation factor, thus eliminating the relaxation factor dependency detected in early versions of momentum interpolation (Majumdar [29]). From Eqs. (33)–(34), u_P and u_E can be rewritten as

$$u_P = \frac{u_P^{**}}{\alpha} - \left(\frac{1-\alpha}{\alpha}\right) u_P^{*} \tag{36}$$

$$u_E = \frac{u_E^{**}}{\alpha} - \left(\frac{1-\alpha}{\alpha}\right) u_E^{*}. \tag{37}$$

Thus, Eq. (35) becomes

$$\begin{aligned} u_e^{**} &= \frac{1}{2}\left(u_P^{**} + u_E^{**}\right) + (1-a)\left[u_e^{*} - \frac{1}{2}\left(u_P^{*} + u_E^{*}\right)\right] \\ &\quad + \alpha\left\{\frac{1}{a_e}(p_P - p_E) - \frac{1}{2}\left[\frac{1}{a_P}(p_w - p_e)_P + \frac{1}{a_E}(p_w - p_e)_E\right]\right\}. \end{aligned} \tag{38}$$

Equation (38) is the form of the momentum interpolation suitable for steady flow problems. The extension of Eq. (38) for unsteady flow problems will include the time-dependent term ($\varrho \Delta x u^o / \Delta t$), where superscript o indicates the previous time value. The appropriate form is

$$\begin{aligned} u_e^{**} &= \frac{1}{2}\left(\frac{a_P}{a_e} u_P^{**} + \frac{a_E}{a_e} u_E^{**}\right) + (1-\alpha)\left[u_e^{*} - \frac{1}{2}\left(\frac{a_P}{a_e} u_P^{*} + \frac{\alpha_E}{a_e} u_E^{*}\right)\right] \\ &\quad + \frac{\alpha}{a_e}\left\{\left(\frac{\varrho^o \Delta x}{\Delta t}\right)_e u_e^o - \frac{1}{2}\left[\left(\frac{\varrho^o \Delta x}{\Delta t}\right)_P u_P^o + \left(\frac{\varrho^o \Delta x}{\Delta t}\right)_E u_E^o\right]\right\} \\ &\quad + \frac{\alpha}{a_e}\left\{(p_P - p_E) - \frac{1}{2}\left[(p_w - p_e)_P + (p_w - p_e)_E\right]\right\} \Delta y. \end{aligned} \tag{39}$$

Although Eq. (39) applies to a 1D, uniform grid situation, it can be easily extended to higher dimensions and nonuniform grids (Lien and Leschziner [24]).

2.3.2. *Cut-Cell Procedures for Solid–Liquid Boundaries*

In accounting for the presence of the internal solid boundaries which define complex geometries on Cartesian grids, the cut-cell approach is applied (Shyy *et al.* [1], Udaykumar *et al.* [12]). In this approach, when the interface passes through the grid, the scenario shown in Fig. 1 is encountered. The control volume designated by P is shown to be cut by the solid surface passing through the grid. The cut-cell procedure rearranges the control volumes in the vicinity of the interface to form a fully consistent mosaic of cells. This is obtained by redefining the interfacial cells (i.e., the control volumes in the vicinity of the interface), so that the control volume fragments lying in each phase are absorbed into appropriate *partner cells*. An

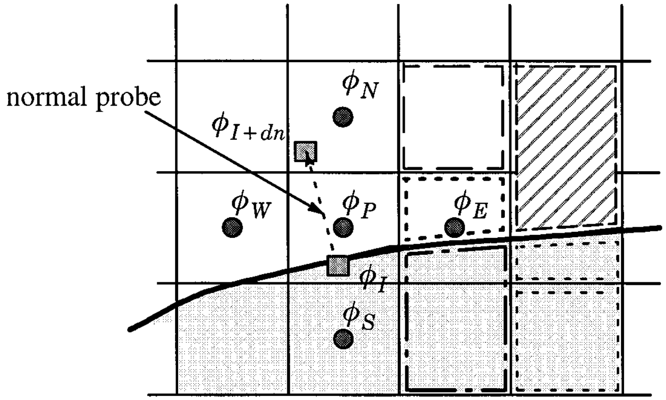

FIG. 5. Illustration of the situation resulting when a complex solid geometry is treated on a fixed Cartesian grid. The cut interfacial cells are reassembled to provide a closed, consistent mosaic to maintain flux conservation. The assembly of cells is performed by absorbing fragments of the control volumes into appropriate cells to reconfigure the cells in the vicinity of the boundary as shown by the dotted lines. Also shown is the normal probe for obtaining gradients at the interface.

example is shown in Fig. 5, where the dotted lines indicate the newly defined control volumes. The fluxes through these redefined control volume faces are thereby evaluated in such a way as to maintain conservation and consistency of the fluxes across each control volume face. For example, the flux of a conserved variable is computed for a cell that is abutted by two neighbors to the left (as in the case of the hatched cell in Fig. 5), in such a way that the flux through the west face of the hatched cell is the sum of the fluxes through the east faces of the abutting cells. This procedure obviates any smearing of information at the interface since the boundary condition (such as no-slip) is imposed at the exact location of the internal boundary in each control volume. This is in contrast to the means employed by Goldstein *et al.* [19] in imposing the no-slip condition. In that work, the no-slip boundary condition is imposed via an external concentrated force field which is computed based on the developing flowfield in the vicinity of the interface. Thus, a feedback control approach is used to compute the shear stresses necessary to obtain a no-slip condition. Information regarding the no-slip surface is redistributed over the finite bound of the δ-function used in the immersed boundary representation of the solid surface.

In the present case, for the evaluation of the source term b in Eq. (23), the diffusion flux from the interface is obtained by describing the field $\phi(x, y)$ for any transport variable such as velocity or temperature. This is done in each phase separately around the interface by means of a biquadratic function and the gradient normal to the interface required in obtaining the diffusion flux is obtained by extending a normal probe from the interface into each phase. The length of the normal is one grid spacing h. This situation is illustrated for the liquid phase in Fig. 5. The value ϕ_{I+dn} at the end of the probe is obtained from the biquadratic function representation in the required phase as $\phi(x, y) = ax^2 + by^2 + cxy + dx + ey + f$. The coefficients are obtained by inverting the 6×6 matrix obtained by the known values of ϕ at six suitably chosen points in the required phase around the end of the probe. The inversion of the matrix is performed by LU decomposition. Thus, the required normal gradient of the field $\phi(x, y)$ is computed as

$$\frac{\partial \phi}{\partial n} = \left(\frac{\phi_{I+dn} - \phi_I}{dn} \right), \tag{40}$$

where dn is the normal probe length of one grid spacing h. The pressure at the solid boundary is obtained by computing the pressure in a similar manner to the above at the reference point and extending the same to the interface, which implies that $\partial p/\partial n = 0$ at the solid boundaries. In the case of the stationary solid boundaries in this work, the convective interfacial fluxes do not contribute to the momentum. However, for moving solid boundaries, the treatment is given in Udaykumar *et al.* [12]. The procedures for the treatment of the internal solid boundaries lead to stable, accurate computations of flows through complex geometries. Some results are presented later in this work.

2.3.3. *The Immersed Boundary Technique for Two-Fluid Interfaces*

When the fluid–fluid interface (i.e., the moving boundary) lies on a fixed grid, some means of communication between the interface and the Eulerian framework for the field equations needs to be devised. One such technique is the cut-cell method described above. In this work, we adopt the immersed boundary technique originated by Peskin [21] and employed extensively by Tryggvason and co-workers (Unverdi and Tryggvason [9], Nobari *et al.* [10], Juric and Tryggvason [13]) for a variety of two-phase flow problems.

In the immersed boundary technique, the presence of the interface and its effect on the flowfield is established by means of source terms in the governing equations; i.e., the information from the Lagrangian interface component is redistributed to the Eulerian framework. For the particular case of two-fluid interfaces under constant interfacial tension, the source term represents the normal stress contribution from the interface. The momentum jump condition, given by Eq. (12) at the interface, is incorporated in the x- and y-momentum equations. Specifically, the contributions to the normal stress balance from the capillarity term in Eq. (12) is redistributed to the surrounding grid points; it is supplied to the source term S_u and S_v in Eqs. (8)–(9). This is done with the aid of a δ-function of bound $4h$, where h is the grid spacing. This procedure leads to the conservative redistribution of the source terms to the grid, due to the properties of the delta function. The discrete delta function at each point in the flowfield assumes the form originally proposed by Peskin [21],

$$\mathscr{D}(\mathbf{x} - (\mathbf{x})_l) = \begin{cases} \dfrac{1}{(4h)^2} \displaystyle\prod_{i=1}^{2} \left(1 + \cos \frac{\pi}{2h} (x_i - (x_i)_l) \right), & \text{if } |\mathbf{x} - (\mathbf{x})_l| \in R \\ 0, & \text{if } |\mathbf{x} - (\mathbf{x})_l| \notin R, \end{cases} \tag{41}$$

where x_i represents the coordinate value and l represents the interfacial marker index. R is set equal to $2h$ in our computations. Each marker contributes to the momentum source term in its proximal control points, i.e., those lying in the circle of radius $2h$ centered at the marker. The force contribution from each interfacial marker to the momentum equations at any point P is given by

$$\mathbf{f}_{Pl} = \kappa_l n_l \Delta s_l, \tag{42}$$

where Δs_l is the arclength corresponding to the lth marker. Thus, the source term in the momentum equations at a given point in the flowfield depends on the proximity of that point to the two-fluid interface. The magnitude of the interfacial forces experienced is dictated by the delta function and is the sum of the contributions of all the interfacial markers lying within the distance of $2h$ from the point. Therefore, the normal stress contribution to the momentum equation is given by the expression

$$\mathbf{F}_p(\mathbf{x}) = \sum_l \mathscr{D}(\mathbf{x} - (\mathbf{x})_l)\mathbf{f}_{Pl}. \tag{43}$$

This procedure of redistribution of interfacial stresses as sources to the field equations leads to the *smoothing* of the discontinuity at the interface. The stability and robustness of this method is enhanced by such smoothing.

The continuity condition at the interface for material interfaces, Eq. (11), is enforced by extracting the normal velocity of the interfacial markers from the grid information by means of a delta function. The δ-function form is

$$\mathbf{V}_l = \sum_i \mathscr{D}(\mathbf{x} - (\mathbf{x})_l)\mathbf{V}_i, \tag{44}$$

where the index i corresponds to the proximal (in the region given by $R = 2h$) grid points. The interface is to be advected with this velocity.

Another feature that needs to be mentioned is the handling of property jumps across the interface. In other approaches using a fixed grid (Kothe *et al.* [5], Sussman *et al.* [6]) some field variable is employed to smooth the property jumps across the interface. Specifically, a Heaviside function is employed such that

$$\mathscr{H}(\phi)_\delta = \begin{cases} 1, & \text{if } \phi > +\delta \\ 0, & \text{if } \phi < -\delta \\ \dfrac{1}{4}\left(\dfrac{\phi}{\delta} + \dfrac{1}{\pi}\sin\dfrac{\pi\phi}{\delta}\right), & \text{otherwise,} \end{cases} \tag{45}$$

where δ is the region of bound $2h$ around the interface. Usually this bound is taken to be proportional to the grid size. Based on the Heaviside function, the material properties are assigned as

$$\beta = \beta_1 + (\beta_2 - \beta_1)\mathscr{H}(\phi)_\delta, \tag{46}$$

where β is any material property such as viscosity and density. The subscripts 2 and 1 indicate the two adjoining phases, in line with our convention for the normal.

In the RIPPLE approach (Kothe *et al.* [5]), which is based on a VOF representation of the phase field, ϕ is taken as a color function dependent on the fluid fraction field, while in the level-set algorithm the ϕ value corresponds to a distance function. In these methods the field variable ϕ is an essential part of the interface tracking procedure. In the immersed boundary technique, Unverdi and Tryggvason [9] employ an indicator function which is obtained by solving a Poisson equation for the entire domain. The indicator function has the characteristics of the Heaviside function, but it has to be computed every time the interface moves. Thus, the calculation of an indicator function involves the solution of an additional field equation and does not fully exploit the available information from the explicitly tracked interface. In our algorithm we have exploited the Heaviside representation to achieve the property smoothing, based on explicit knowledge of the interface and the two types of information indicated in Section 2.1.1 above. Once the marker locations with respect to the grid are known, the property jumps can be assigned, based on the Heaviside function. In the present case, the Heaviside function takes the form

$$\mathscr{H}(\mathbf{x}-(\mathbf{x})_l) = \begin{cases} \dfrac{1}{4}\displaystyle\prod_{i=1}^{2}\left(\dfrac{x_i-(x_i)_l}{\delta}+\dfrac{1}{\pi}\sin\dfrac{\pi}{\delta}(x_i-(x_i)_l)\right), & \text{if}\,|\mathbf{x}-(\mathbf{x})_l|\in R,\\ 1, & \operatorname{sgn}(\mathbf{x}-(\mathbf{x})_l)\,|\mathbf{x}-(\mathbf{x})_l|<-\delta,\\ 0, & \operatorname{sgn}(\mathbf{x}-(\mathbf{x})_l)\,|\mathbf{x}-(\mathbf{x})_l|>+\delta, \end{cases} \tag{47}$$

where $(x_i)_l$ represents the coordinate of the interfacial point where the Heaviside function is required. The smoothing of the material properties is performed with Eq. (46) above.

The material properties in the bulk of the phases are assigned first. Thereafter the transition region between any two phases is smoothed by defining the Heaviside function locally in this region. To accomplish this, one traverses along the interface and modifies the value of the material property according to Eq. (46), in the cells adjoining the interface and lying within the bound $\delta = 2h$ of the interface. These operations are confined to the region close to the interface only, hence relieving the computational burden. This procedure for smoothing material discontinuities holds when there are multiple interfaces, including cases in which interfaces may enclose other interfaces.

2.4. Mass Conservation in Individual Phases

In the scheme presented above, the interaction of the interface tracking algorithm, as provided by the immersed boundary technique, with the flow solver does not enforce conservation of mass in the phase enclosed by the interface. This is because the divergence-free velocity field is enforced in each control volume by the flow solver; the velocity employed to evolve the interface is interpolated from such a velocity field. This interpolated velocity field may violate the divergence-free condition, resulting in a mass leak from the phase enclosed by the interface. Peskin and

Printz [30] suggest a method based on the modification of the divergence operator in order to enforce mass conservation. In our work, we choose to achieve the same result by enforcing mass conservation in our iterative solution process so that the correct level of hydrostatic pressure is induced in the enclosed phase. This is done in the following way. In order to satisfy the mass constraint we require, in each enclosed phase,

$$m_{\text{bubble}} = \int_0^{s_{\max}} \varrho H_y \frac{\partial x}{\partial s}\, ds = \text{const}, \tag{48}$$

where H_y is πy^2 for the axisymmetric case and y for the planar case, ϱ is the density of the fluid inside the enclosed mass, such as a droplet, s is the arclength, and $s_{\max}$ is the total arclength of the curve representing the boundary of the enclosed mass. In Eq. (48), a bubble is used as the example; obviously, the same procedure is applicable to other cases, such as a droplet. Since the pressure correction formulation only provides an estimate of the pressure gradients necessary to satisfy the continuity equation cellwise (i.e., across control volume faces), global conservation information is not provided by this means. Thus, the continuity constraint as expressed by the pressure correction equation establishes the hydrodynamic part of the pressure inside the enclosed mass consistent with the flowfield, but it provides no information regarding the hydrostatic component. The dynamic form of the Young–Laplace equation at the interface establishes the normal stress balance as

$$\Delta(p_d + p_c) + \Delta(\text{viscous terms}) = \gamma(\kappa_1 + \kappa_2), \tag{49}$$

where Δ represents the jump across the interface and the viscous terms take the appropriate forms in planar and axisymmetric cases, as given in Eqs. (7)–(10). In the above equation, subscript d indicates the hydrodynamic parts and c the hydrostatic parts of the pressure. In the formulation presented here, the incorporation of the surface tension terms in the momentum equations leads to the establishment of the balance in Eq. (49). However, there is a missing component in the pressure, namely p_c, which needs to be obtained to satisfy the mass constraint. Kang and Leal [2] indicate the appropriate correction to the p_c term as a time-dependent value $C(t)$ which needs to be computed to satisfy the mass constraint. This parameter $C(t)$ arises when the pressure at the interface is obtained by integrating the component of the momentum equations in the direction tangential to the interface in each phase. This is easier to see in the case where the flow on each side of the droplet is obtained separately and then matched at the interface through the jump condition Eq. (12), as is the practice in the boundary-fitted formulation employed by Kang and Leal [2]. In related work, the practice of rescaling the interface shape periodically to maintain the enclosed mass constant was adopted (Stone and Leal [31]). In the work presented by Nobari *et al.* [10], it is mentioned that the mass of droplets is maintained, but the mechanism by which this is established by their solver is not clear. In recent work on the dynamics of menisci in crystal growth, Shyy and Rao [32] have, with the pressure-correction methodology used here, maintained the volume of the meniscus by employing an iterative procedure to obtain the proper value of the hydrostatic pressure, consistent with Eq. (49) as well as mass conservation. However, the computations used the boundary-fitted technique and need to be modified in the present context.

A method for correcting the hydrostatic pressure in the enclosed mass needs to be devised so that it does not lose or gain mass. To achieve this goal, we devised an indirect method of establishing mass conservation similar to that adopted by Kang and Leal [2]. The desired result in enforcing mass conservation is to establish an additive constant to the pressure inside the enclosed mass. Upon correction we desire the balance:

$$\Delta(p_d + p_c + \delta p_c) + \Delta(\text{viscous terms}) = \gamma(\kappa_1 + \kappa_2 + \delta\kappa). \tag{50}$$

Here the correction to the pressure δp_c is responsible for changes in the droplet shape represented by $\delta\kappa$ so that upon integrating as in Eq. (48) over this new shape, the volume is conserved. In our procedure, during the iterative process of establishing the flowfield, we impose the mass constraint on the interface motion by establishing the shape correction $\delta\kappa$ and inducing the correct pressure increment δp_c. At each iteration, this shape correction is performed after the interface has been advected to its new position based on the kinematic condition. Thus the fresh iterate of the x-coordinate of interfacial marker position is obtained by

$$\begin{aligned} (X_l^{N,k+1})_p &= X_l^k + \delta t\, V_n\, n_x \\ (X_l^{N,k+1})_c &= (X_l^{N,k+1})_p + \delta_n\, n_x, \end{aligned} \tag{51}$$

where subscripts p and c represent predicted and corrected values, subscript l is interfacial marker index, superscripts N and k represent the iteration number and time step, respectively. Corresponding expressions apply for the y-coordinate. The shape correction in the normal direction δ_n is performed in an iterative fashion by means of a bisection method, so that the mass of the droplet as computed from Eq. (48) is maintained a constant. The value of δ_n is obtained from the knowledge of the arclength measure of the interface, already established in the course of calculation, and the estimate of the mass loss. Specifically, the bisection method used to obtain the value of δ_n can enforce mass conservation and enable the procedure to converge in a few iterations (typically <5). The entire mass conservation measure is enclosed in the outer iteration loop for the entire solution procedure, including interface movement, flowfield computation, and mass constraint imposition. The procedure is then required to achieve a preset tolerance for convergence levels of the flowfield, interface shape, and enclosed mass. It should be emphasized that the present procedure is of a predictor–corrector type, and at convergence should yield a droplet shape independent of the manner δp_c is imposed.

3. RESULTS AND DISCUSSION

In this section we seek to illustrate the accuracy and versatility afforded by the combination of the cut-cell method and the immersed boundary technique. Towards this objective, we first present test cases to evaluate the performance of the cut-cell method in the current collocated-variable framework. This cut-cell approach was tested in previous work (Shyy *et al.* [1], Udaykumar *et al.* [12]) for the staggered variable arrangement. The second step is to compare the results for the immersed boundary technique in the present finite-volume, pressure-based framework for droplet dynamics. For this particular application, reliable experimental and numerical results exist, at least for highly viscous flow, with which we compare our results. Finally, we put the cut-cell and immersed boundary representations together to enable the simulation of droplet dynamics in a constricted tube. This last aspect demonstrates the ability of the present method to handle multifluid flows in arbitrary geometries under viscosity- or inertia-dominated flow conditions.

3.1. Flows with Fixed Arbitrary-Shaped Internal Boundaries

One objective of this work is to develop a facility for computing flows in complex geometries on Cartesian grids. This feature will remove restrictions regarding the flow domains in which the moving boundary simulations can be performed, without having to resort to body-fitted grids or unstructured grid layouts. We first compare solutions for a stationary interface with those from well-tested solution procedures using body-fitted coordinates (Shyy [26]). In both cases, the second-order central difference scheme is used to discretize the convection, diffusion, and pressure gradient terms in the momentum equations. This is one of several exercises performed to validate the conservation and consistency characteristics of the cut-cell method used to treat the complex geometry. The interface is sufficiently deformed that all the possible types of cut cells are encountered. The square cavity is a frequently adopted test bed for numerical experiments for incompressible flows and benchmarked solutions exist. We deform the base of the cavity, the amplitude being 10% of the base. A 121×121 Cartesian grid is employed. We first present the results for a driven cavity flow, where the top wall of the cavity is pulled at velocity $U = 1$ corresponding to a Reynolds number of 1000. The results from the present method are compared with a previously benchmarked body-fitted staggered grid formulation (Thakur *et al.* [33]) with the same grid size. The results are shown in Fig. 6. The streamline pattern is shown in Fig. 6a. A quantitative comparison can be seen in Figs. 6b and 6c, where the centerline velocities are plotted. As seen in this figure, the centerline profiles obtained from the cut-cell technique using the collocated grid (solid line) agree well with the body-fitted staggered grid calculations (open circles). Results for problems involving natural convection are presented in Udaykumar *et al.* [12].

We next demonstrate the ability of the complex geometry treatment to simulate more complex flow situations. In Fig. 7, the streamlines and pressure contours for a driven cavity with top and bottom moving walls and enclosing a semicircular cavity at the bottom wall are shown. The smaller cavity is indicated with dotted lines in Fig. 7, which represents a solid boundary with zero internal thickness. This configuration gives an indication of the versatility of the present algorithm. Figure 7a shows the streamlines and 7b shows the pressure contours in the two cavities. As can be seen from the figure, for the Reynolds number of 1000, the multiple

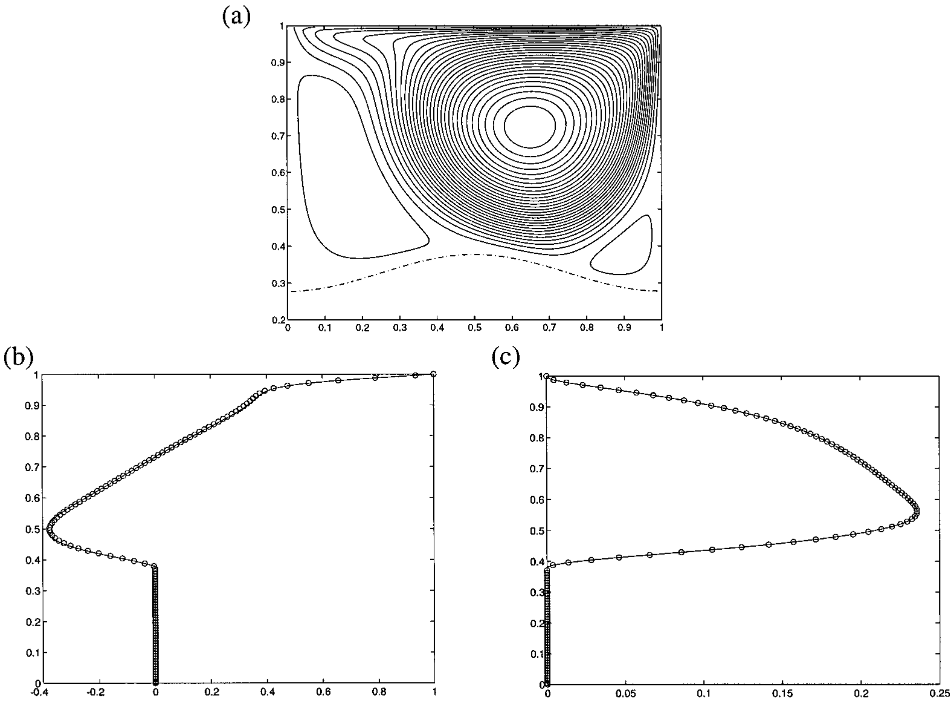

FIG. 6. Comparison of a deformed cavity at Re = 1000, for results using the cut-cell technique on the collocated grid with the solution on a boundary-fitted staggered grid. (a) Streamline contour for the collocated grid. (b) u-velocity along vertical centerline for the present collocated grid case (solid line) and the staggered grid case (open circles). (c) v-velocity comparison along vertical centerline.

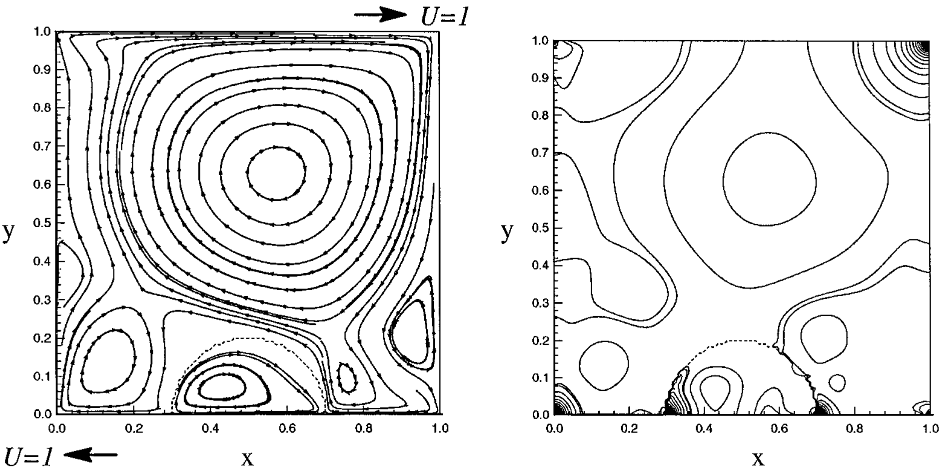

(a) Streamline (b) Pressure

FIG. 7. Double-driven cavity flow with obstruction. $R_e = 1000$, 121×121 grid. Dotted line shows the shape of the enclosed cavity.

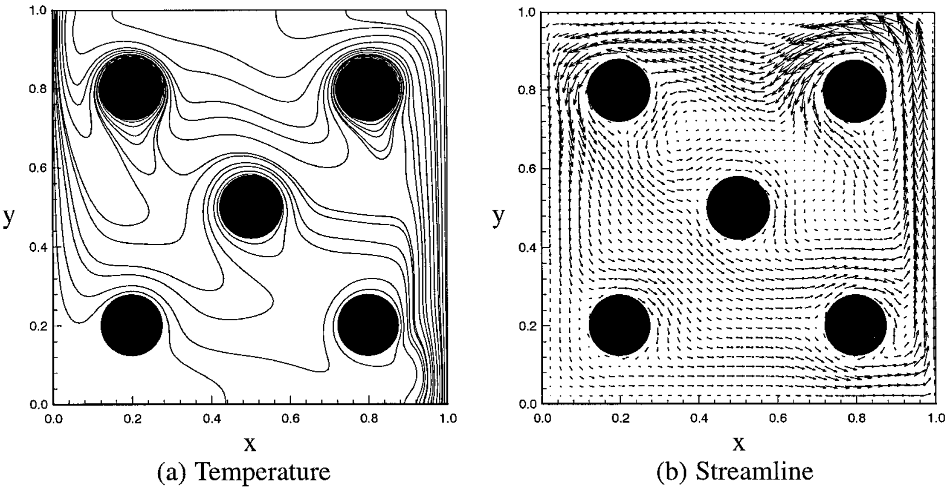

FIG. 8. Natural convection flow in a cavity. Pr = 1, Ra = 10^6, 121 × 121 grid.

recirculation zones, including the one in the smaller cavity, are well captured. It would be a significant task to fit a good boundary-fitted grid to this configuration. An added advantage that may be realized is that the grid can be refined easily in the present Cartesian framework without consideration of the solid boundary shape or the number of solid boundaries present.

Figure 8 shows the results of a natural convection flow in a square cavity with multiple objects in the flowfield. The sidewalls of the cavity are heated, the nondimensionalized temperature of the left wall is maintained at 0 and that of the right wall at 1. The top and bottom walls are adiabatic. Each of the cylinders is maintained at a constant temperature of 0. A Prandtl number of 1, Rayleigh number of 10^6 flow was computed. In Fig. 8a we show the isotherms and in 8b, the velocity vectors. The skew-symmetry of the temperature field, obtained in such a cavity without obstacles, is broken by the placement of the five shapes. In particular, the temperature gradients in the right bottom corner appear to be enhanced by the presence of the cylinder in that location while those in the lower left corner are diminished. This would obviously have a significant impact on the heat transfer within the cavity shown. This type of facility would be useful in computing heat transfer around complex geometries and can be combined with phase change as demonstrated in Udaykumar *et al.* [12]. No restriction exists on the number or shape of the obstructions that can be inserted in the domain. Since all the measures dealing with the interior solid boundaries are handled by means of one-dimensional arrays, the expense of incorporating internal boundaries varies linearly with the number of objects. No grid generation measures are required when a new object is introduced, thus objects can be added or deleted without affecting the existing geometry globally.

Finally, a transient calculation is performed in an open channel configuration. The case shown in Fig. 9 demonstrates the usefulness of this procedure for the time-dependent case. Here, the inlet is at the left of the domain. The Reynolds number in this case is 100. A 121 × 81 grid is used. The development of the recirculation zone behind the cylinder is shown until a steady state is reached at

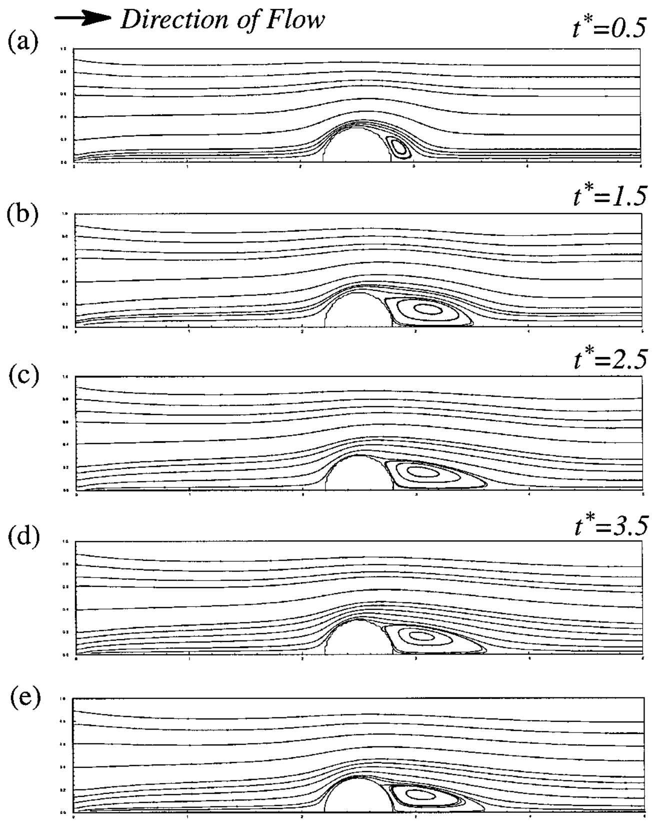

FIG. 9. Open channel flow, transient calculation. $\mathrm{R_e} = 100$, 121×81 grid. (a) to (d) Streamline plot showing development of the steady recirculating flow behind the cylindrical obstruction computed using the cut-cell method. (e) Steady-state streamlines from the body-fitted calculation.

nondimensional time $t = 3.5$. In Fig. 9e, we show the streamlines obtained for this geometry from a steady-state calculation on a well-tested boundary-fitted staggered grid (Thakur *et al.* [33]). The flowfields obtained from the two methods are identical. In particular, the recirculation zone in each case extends up to $x = 3.61$ in the rear of the cylindrical obstruction. The slight differences in the streamlines between (d) and (e) are due to the differences in data representation on the Cartesian and curvilinear grids which is interpreted differently by the contouring facility. It is also noted that the cylindrical obstruction has been shown in this figure by means of a phase fraction contour. The step-like nature of the obstacle is a limitation of the contouring procedure. As far as the solver itself is concerned, the surface is represented smoothly by means of the cut-cell technique.

3.2. Moving Boundary Flow Problems

3.2.1. *Deformation of Viscous Droplets in Axisymmetric Extensional Stokesian Flow*

We now present results for the droplet deformation studies. A straining flow is imposed on the droplet and the Stokes equations are solved. The nondimensionalization of the governing equations is performed using the reference quantities as described below.

We define the viscosity ratio between droplet and suspending fluids as $\lambda = \mu_i/\mu_o$. The characteristic velocity, length, pressure, and viscosity are the following: $u_c = \gamma/\mu_c$, $l_c = a =$ the radius of undeformed circular shape, $p_c = \mu_c u_c/l_c$, $\mu_c = \mu_o =$ the viscosity of the suspending fluid, and γ is the droplet surface tension. Then, the dimensionless governing equations for creeping flows become:

Continuity equation,

$$\nabla \cdot \mathbf{V} = 0; \tag{52}$$

Momentum equation for suspending fluid,

$$0 = -\nabla p + \nabla^2 \mathbf{V} + \int \kappa \mathbf{n} \delta(\mathbf{x} - (\mathbf{x})_l)\, ds \tag{53}$$

for the droplet,

$$0 = -\nabla p + \lambda \nabla^2 \mathbf{V} + \int \kappa \mathbf{n} \delta(\mathbf{x} - (\mathbf{x})_l)\, ds; \tag{54}$$

and the far field condition for planar flow is

$$\mathbf{V}_\infty = \frac{\mathrm{Ca}}{2} \begin{pmatrix} 2 & 0 & 0 \\ 0 & -2 & 0 \\ 0 & 0 & 0 \end{pmatrix} \cdot \begin{pmatrix} x \\ y \\ z \end{pmatrix} \tag{55}$$

and for axisymmetric flow,

$$\mathbf{V}_\infty = \frac{\mathrm{Ca}}{2} \begin{pmatrix} 2 & 0 & 0 \\ 0 & -1 & 0 \\ 0 & 0 & -1 \end{pmatrix} \cdot \begin{pmatrix} x \\ \theta \\ y \end{pmatrix}, \tag{56}$$

where the capillary number Ca arises from the nondimensionalization and is given by $(\mu_c G a/\gamma)$. (G is the strain rate of the imposed flow.) The discretization of the above equations is described in Section 2.3. The flow condition and grid layout is indicated in Fig. 10. The grid distribution is nonuniform; in the farfield, i.e., away from the inner region shown, the grids are stretched linearly toward the boundaries of the domain, while in the inner region a uniform fine grid is used. This yields better resolution in the desired region of the flowfield, i.e., in the vicinity of the interface. The flowfield is imposed as shown, thereby exploiting the symmetry of the problem. The incoming flow at the top and outgoing flow at the right are held constant as specified by Eq. (55) and Eq. (56) for planar and axisymmetric cases, respectively. The distribution of markers along the interface is maintained at a constant arclength spacing. The arclength spacing used in all computations presented

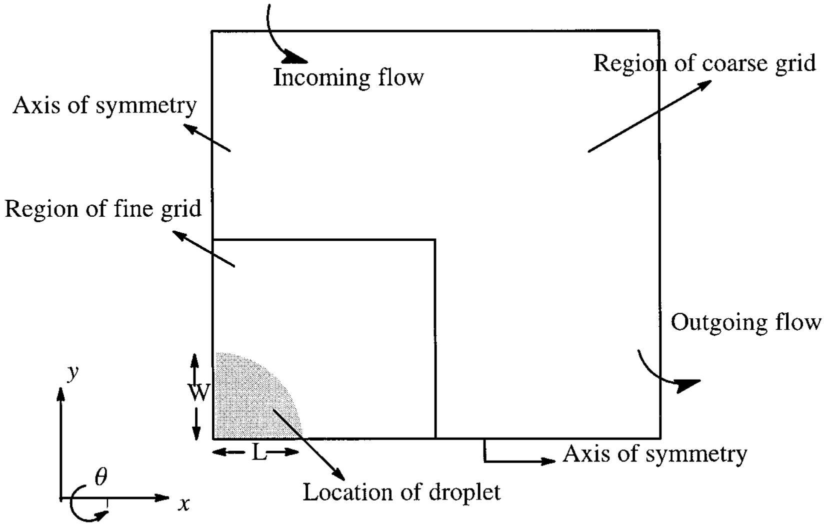

FIG. 10. Illustration of domain of computation and boundary conditions for droplet deformation simulation.

here is $0.8h$, which was found by experimentation to provide adequate resolution and accuracy. The redistribution along the interfacial curve is performed at every time step to prevent undesirable depletion or accumulation of markers.

At the outset, a suitable grid is determined for the moving boundary simulations. A grid independence study was first performed to obtain the steady-state shapes of the droplet in extensional flow at a capillary number of 0.1, which is slightly below the critical capillary number. In Fig. 11, we compare the results obtained from calculations on an 81×81 and 161×161 grid with and without mass conservation. As can be seen, the results from the two grids with mass conservation imposed are in close agreement. We henceforth retain the same grid density as that corresponding to the 81×81 grid in the present case. The number of grid points will therefore scale with the domain size.

The moving boundary capability using the immersed boundary technique is first tested against the results of Stone and Leal [31, 34] for steady axisymmetric droplet shapes in a uniaxial extensional flow. For a range of capillary numbers below the critical capillary number $\mathrm{Ca}_{\mathrm{cr}}$ the droplet deformation culminates in a steady-state shape. Stone and Leal [31] have proposed that the deformation parameter $D = (L - W)/(L + W)$ is an indicator of the final bubble shape at steady state, where L is the major radius and W is the minor radius of the ellipsoidal droplet as shown in Fig. 10. This quantity therefore provides an estimate of the aspect ratio of the steady-state shape.

In Fig. 12, we compare the D vs. Ca curves obtained from our calculations with those of Stone and Leal [31, 34] for viscosity ratio $\lambda = 1$. The grid in this case was 61×61 in the inner region of dimensions 3×3 units. The arclength spacing of the interfacial points, following testing to determine accuracy, was fixed to be $0.8h$ in this and following calculations. The number of points on the interface was 45 at

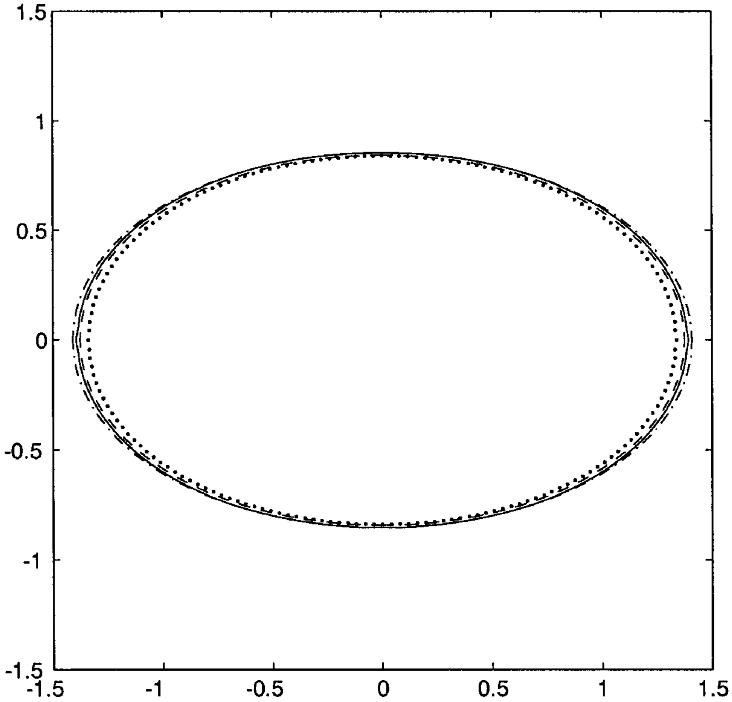

FIG. 11. Grid independence test for Ca = 0.1. The final steady-state shapes are shown for (a) ....., 81 × 81 grid without mass conservation; (b) --, 161 × 161 grid without mass conservation; (c) —, 81 × 81 grid with mass conservation; (d) -.-, 161 × 161 grid with mass conservation.

steady state. As can be seen from the figure, our results are in good agreement with those of Stone and Leal [31]. Furthermore, the critical capillary number of $\mathrm{Ca}_{\mathrm{cr}} = 0.12$ obtained in the present case also corresponds to the value in Stone and Leal [31].

Figures 12b and c show the flowfield and pressure contours in the case of Ca = 0.1. It is clear from the velocity vector plot that the flow at steady state is tangent to the surface of the droplet and the single-domain treatment of the interfacial forces yields the desired shape and flowfield by the balance of normal stresses in Eq. (12). The large pressure gradient across the interface is also seen clearly in this figure.

We next study the unsteady deformation and recovery characteristics of droplets under imposed straining flow with $\mathrm{Ca} > \mathrm{Ca}_{\mathrm{cr}}$. The inner region of fine grid in this case is 6 × 6 units. The domain of computation is 8 × 8 units in size. In the inner region 121 × 121 grids are used, while in the coarse grid region 20 points are used along each direction and the grid is linearly stretched. In Fig. 13a, we show the shapes of the droplet at different times for the Capillary number of 0.14. In this case, the droplet deforms to a maximum extent of 5.4 times the initial radius at nondimensional time $t = 35$. The number of points on the interface increases from 27 initially to 140 at the final stage. To study the recovery of the droplet, we turn off the flow at the stages corresponding to the shapes at $t = 28$ and $t = 35$ and

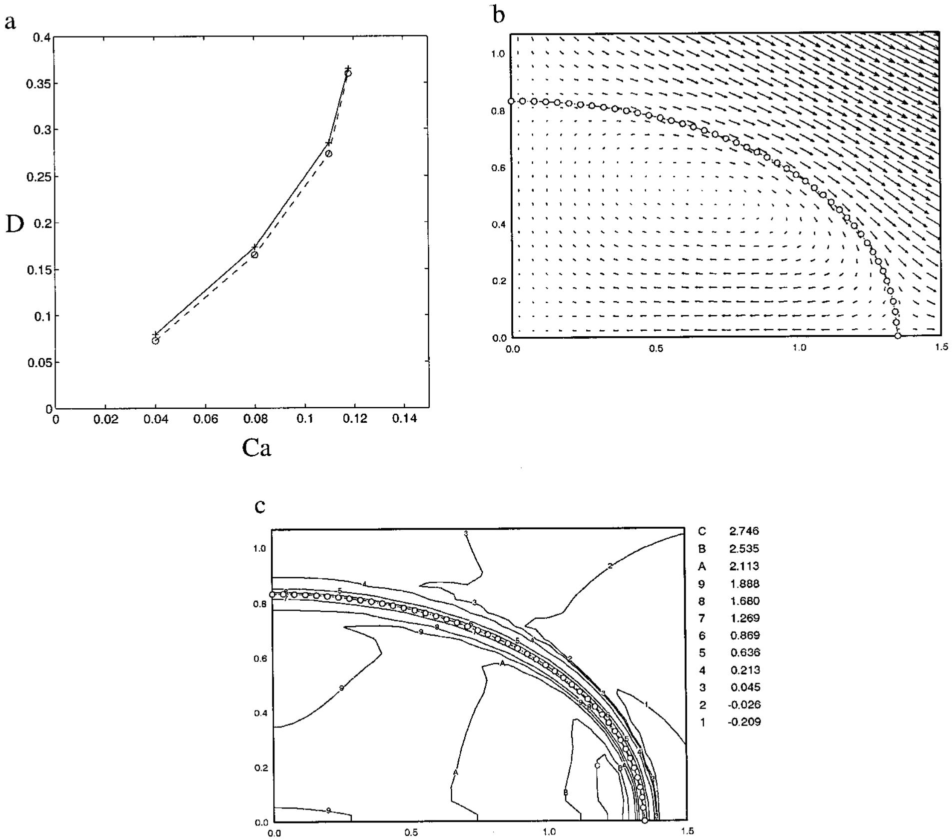

FIG. 12. (a) Comparison of $D = (L - W)/(L + W)$ vs. Ca obtained from the present method (solid line) with the results (dashed line) of Stone and Leal [31]. The critical capillary number is approximately 0.12 in both studies. (b) Velocity vectors at steady state for Ca = 0.1. (c) Pressure contours at steady state for Ca = 0.1.

track the recovery path in the two cases. The results are presented in Figs. 13b and c, respectively. As can be seen, for the smaller deformation case the interface recovers back to the spherical droplet shape, while for the larger deformation case, the recovery process results in the impending breakup stage shown. Although the further development of the droplet after this stage can be handled by the code, we stop the computations at this stage. From Fig. 13b, it is seen that the droplet returns to a sphere of radius 1, which demonstrates that the mass conservation procedure implemented holds well in the course of the large deformations experienced by the droplet. It may be surmised from Figure 13c that a small satellite droplet is formed along with two larger droplets in the recovery from the large deformation. This behavior of the droplets with extent of deformation for the same capillary number is in qualitative agreement with the results of Stone and Leal [34].

In Fig. 14, we show the flowfields resulting from the computations. In Fig. 14a, at left are the velocity vectors and at right the pressure contours for the final shape of the interface ($t = 35$). As can be seen, the flow in this case tends to draw the

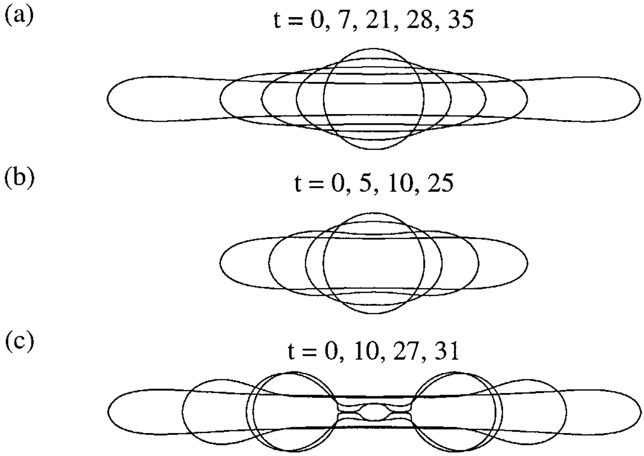

FIG. 13. Deformation and relaxation of the droplet for capillary number of 0.14 (critical capillary number is 0.12). (a) Deformation stage, shapes shown at $t = 0, 7, 21, 28$, and 35. At $t = 38$ the deformation is 5.4 times the original undeformed radius. (b) Recovery of the droplet from shape shown at $t = 28$ in (a). (c) Recovery of the droplet from shape shown at $t = 35$ in (a).

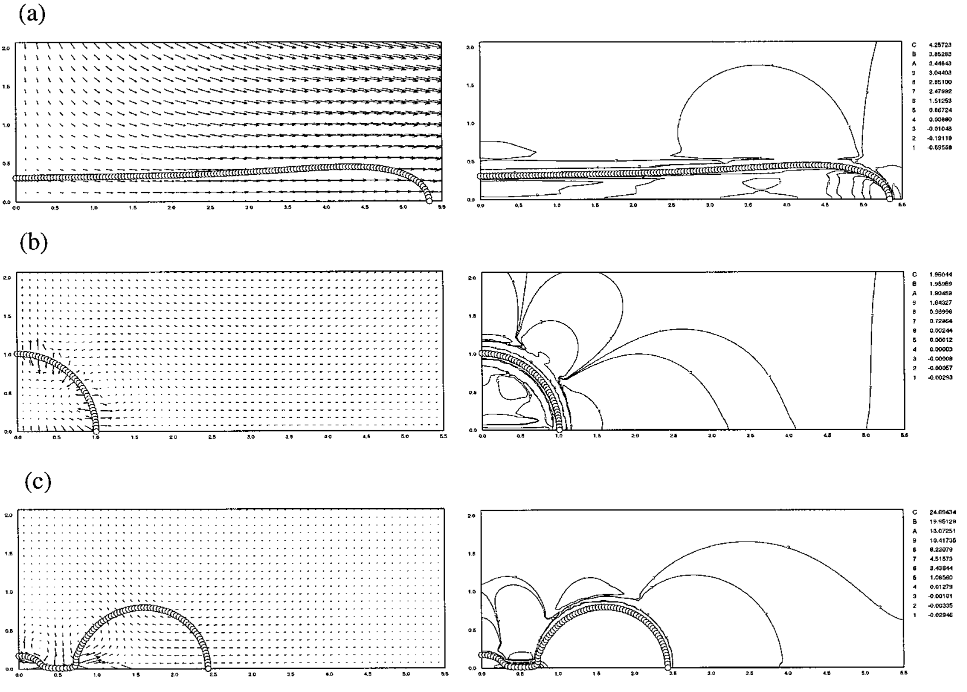

FIG. 14. Left row—velocity vectors (a) at the times $t = 35$ in Fig. 13(a); (b) the final interface location in Fig. 13(b); (c) the final interface location in Fig. 13(c). Right row—pressure contours corresponding to the above.

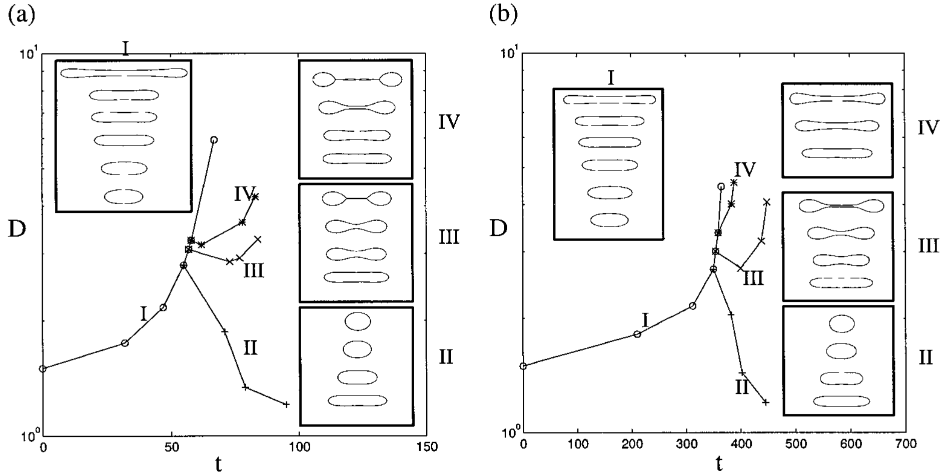

FIG. 15. Recovery curves for viscous droplet subjected to uniaxial extensional flow as a test of the accuracy of the method for large deformations and property jumps. (a) The recovery curve for $\lambda = 1.0$. (b) Recovery curve for $\lambda = 10$.

droplet out into a filament. In Fig. 14b, the velocity vectors for the recovered shape after release from the smaller deformation are shown. The velocity magnitudes are very low ($O(10^{-4})$) in this nearly quiescent state of the flowfield. The corresponding pressure contours are shown at right. It can be seen that the pressure levels inside the droplet are uniform and equal to approximately 1.96 in value, which is close to the expected static value for the given initial droplet shape. In Fig. 14c, the velocity vectors and corresponding pressure contours for the final interface shape in the evolution of the droplet in Fig. 13c are shown. The impending breakup of the droplet is evident from the large velocity and pressure values observed in this figure. The capillary induced flow which results in the breakup of the droplet is clearly seen in regions of large negative curvature in Fig. 14c. Due to the lack of resolution in the region of breakup, the values in this figure are not of significance. It is noteworthy that the collocated grid solution framework holds up in the presence of the large pressure gradient seen in this case (maximum pressure value = 24; minimum = −0.8).

In Fig. 15, we present the recovery characteristics of viscous droplets in uniaxial extensional flow for the viscosity ratios $\lambda = 1.0$ and 10.0. In Fig. 15a, we plot the deformation of a droplet for the case of Ca = 0.13, which is slightly above the critical capillary number, and $\lambda = 1.0$; i.e., the viscosities of the droplet and the suspending fluid are the same. The droplet is deformed to a certain L and a step change in the flow to Ca = 0.065 is made. The step change in the imposed flow strength is made at three different points along the deformation curve. The shapes along the deformation and recovery curves are also shown in the inset boxes. These curves seek to demonstrate the accuracy of the present calculations for long periods and large magnitudes of droplet deformation. The results here are in agreement with those of Stone and Leal [34]. In particular, the fate of the recovering droplets from three different initial deformations, following a step change in the flow strength match with the predictions in Stone and Leal [34]. The initial large deformation of the droplet due to stretching is evident in the inset marked I. When the released droplet takes path II, i.e., for a L value before release of 2.79, the droplet recovers to a steady-state shape corresponding to Ca $= 0.065$. For a value of $L = 3.07$, no recovery is possible. In this case, as can be seen in the recovery curve, the droplet initially shrinks. However, during this process a waist develops at the equator of the droplet and results in the extension of the droplet as the flow induced by the capillary forces accompanying this negative curvature drives the fluid outward, as seen in the extreme case in Fig. 14c. This situation is unstable and leads to the further development of the waist and subsequent breakup of the droplet. Thus, droplet breakup in such flows is dependent on the competition between the imposed flowfields and the flow induced by capillarity. Therefore, although a waist exists in the deformation curve marked I, in this situation the flows due to stretching and capillarity reinforce each other, while in the recovery phase they oppose each other. The result of the recovery process depends on the strength of the destabilizing flow induced by the capillary forces acting at the waist, which depends on the curvature at the waist. In Fig. 15b, for example, it is seen that the droplet in case IV, which represents $L = 3.24$ before release, rapidly heads toward breakup. This is in contrast to the other cases, where there is an initial tendency to respond to the imposed flowfield before capillarity takes over. It is therefore clear that questions regarding recovery, the number of droplets resulting from breakup, the sizes of droplets, and so on, can only be answered in the context of the flowfields imposed, relative properties of droplets and suspending fluids, and the extent of deformation.

The rates of deformation obtained from our calculations agree very well with those in Stone and Leal [34]. Some differences in times of deformation exist between the two calculations in the initial phase of the deformation. These may be due to the differences in initial conditions or capillary numbers chosen for the deformation. A notable point is that the time scale of deformation of droplets in viscous extensional flows is expected to be proportional to $(1 + \lambda)$ (Stone and Leal [31]). A comparison between Figs. 15a and b reveals the validity of this scaling.

3.2.2. *Deformation of Droplets in Extensional Flows with Inertia Effects*

In order to demonstrate the ability of the algorithm to deal with convective droplet dynamics, we investigate the effects of an imposed uniaxial extensional flow. The scales chosen for this problem are the same as the ones for the viscous droplet presented in the previous section. However, in this case, with the inclusion of the convection terms, the nondimensionalized governing equations are

Continuity equation,

$$\nabla \cdot \mathbf{V} = 0; \tag{57}$$

Momentum equation for suspending fluid,

$$\frac{\partial \mathbf{V}}{\partial t} + \nabla(\mathbf{V}\mathbf{V}) = -\nabla p + \frac{1}{R_e}\nabla^2\mathbf{V} + \frac{1}{W_e}\int \kappa\mathbf{n}\delta(\mathbf{x} - (\mathbf{x})_l)\, ds \tag{58}$$

for the droplet,

$$\beta\left(\frac{\partial \mathbf{V}}{\partial t}+\nabla(\mathbf{V}\mathbf{V})\right)=-\nabla p+\frac{\lambda}{R_e}\nabla^2\mathbf{V}+\frac{1}{W_e}\int \kappa\mathbf{n}\delta(\mathbf{x}-(\mathbf{x})_l)\,ds. \tag{59}$$

Under convective conditions the relevant nondimensional parameters that arise are the Reynolds number ($\mathrm{Re} = 2\varrho_c(Gl_c)l_c/\mu_c$, where l_c is the droplet radius) and the Weber number ($\mathrm{We} = 2\varrho_c(Gl_c)^2l_c/\gamma$). The former provides a measure of the relative dominance of inertia to viscous effects, while the latter is the ratio of inertia to capillary forces. In the results presented the imposed flow corresponds to a Reynolds number of 10. $\beta = \varrho_i/\varrho_o$ denotes the density ratio and $\lambda = \mu_i/\mu_o$ is the viscosity ratio.

We attempt to obtain the critical Weber number for a droplet under such an imposed linear flow condition. Kang and Leal [2] have obtained the critical Weber number of a bubble at this Reynolds number as lying between 0.9 and 1.0. In that work, the density and viscosity inside the bubble was considered to be negligible so that the pressure inside the bubble remains a constant, and the interior of the bubble is passive, in that it has no effect on the deformation characteristics. Under this assumption they fit a boundary-conforming grid to the exterior of the bubble and obtained the transient deformation characteristics of the bubble surface. This treatment is a limitation imposed by the boundary-fitted grid approach. If calculations were to be performed inside the bubble also, grid-generation would become complicated. In our framework this limitation does not exist. On the other hand, in the present framework, it is not a simple matter to render the flowfield inside the bubble entirely passive, since the present method is a single-domain method. This rendering of a part of the domain passive was accomplished in previous calculations involving stationary and moving solid boundaries, where there is no flow in the solid region. In the case of two-fluid interfaces this is not as straightforward to do, due to the fact that the interface velocity is governed by the kinematic condition at the boundary and the boundary velocity is obtained from a single-domain formulation, Eq. (44). Thus information regarding the velocity field is required from both sides of the interface, which means that the flowfield needs to be computed in both phases. Therefore, in performing our calculations in this section we will only be able to obtain a qualitative comparison with Kang and Leal [2], and we will support our result with expectations based on the physics of the problem. The flow configuration remains the same as shown in Fig. 10. The density and viscosity ratios used are $\beta = \varrho_i/\varrho_o = 0.02$ and $\lambda = \mu_i/\mu_o = 0.02$, respectively.

In Kang and Leal [2], it was shown that the deformation of the droplet, in particular the availability of a steady-state solution for a given Weber number was dependent on the initial state of the droplet in the flowfield. Therefore, although for certain Weber numbers close to, but below, critical, gradually increasing the flow strength from a lower Weber number yielded steady-state solutions, imposing a step change in the flowfield could drive the droplet toward unsteady, continuous stretching. Such behavior was noticed in our simulations also. Therefore, for the cases presented here, we obtained the flow at a given We, *under a particular combination of density and viscosity,* starting from the flowfield corresponding to a value of We 0.1 lower. The curves in Fig. 16a show the variation of D and We for the imposed flow at $\mathrm{Re} = 10$. To start these curves, we first obtained the flowfield

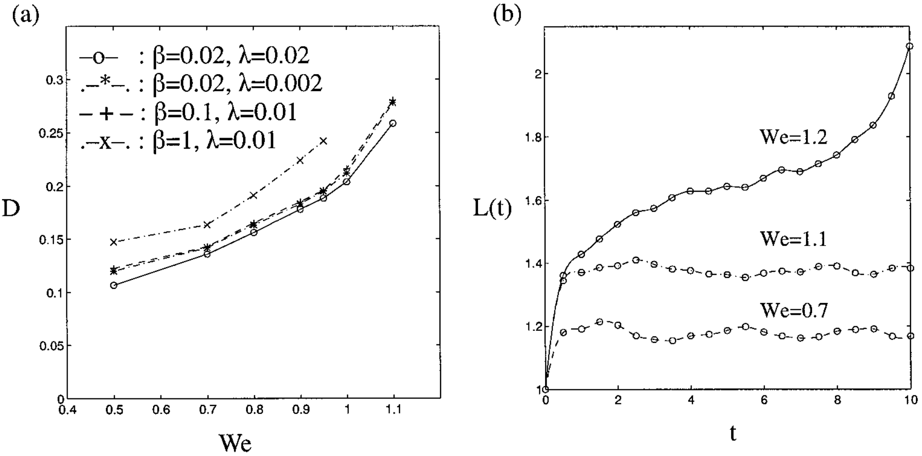

FIG. 16. Deformation of a bubble under uniaxial extensional flow at Re = 10. (a) Curves show the deformation parameter D vs Weber number We with different fluid properties. The critical Weber number varies from case to case. (b) L vs t plot (for $\beta = 0.02$, $\lambda = 0.02$) with three different Weber numbers (We = 0.7, 1.1, 1.2).

at We = 0.5 by imposing a flowfield instantaneously. This led to an oscillation of the droplet due to the competition between inertia and capillarity effects. This type of behavior is also reported by Mashayek and Ashgriz [35]. For example, for $\beta = 0.02$ and $\lambda = 0.02$, upon imposition of the flowfield the droplet at We = 0.5 stretches rapidly from its initial circular shape to a value along the x-axis of $L = 1.4$, and subsequently relaxes in an oscillatory manner to a steady-state value of $L = 1.17$. Stepping up the Weber numbers in increments of 0.1 thereafter yields the curve shown in Fig. 16a. For $\beta = 0.02$ and $\lambda = 0.02$, and at a Weber number of 1.2, a steady state did not exist. If these fluid properties are changed, then the critical Weber number changes accordingly. A closer examination of the case of $\beta = 0.02$ and $\lambda = 0.02$ can be seen from the curves of L versus t shown in Fig. 16b, where the deformation histories for We = 0.7, 1.1, and 1.2 are plotted. As can be seen, these curves show the oscillatory relaxations mentioned above. However, in the case of We = 1.2, the oscillations carry the interface away from a steady state and instability results. As pointed out in Ryskin and Leal [36], the critical Weber numbers for bubbles ($\beta \rightarrow 0$, $\lambda \rightarrow 0$) and droplets are expected to be different. In our cases, we expand the parameter range of the density and viscosity combinations. To gain more insight, the following description is given.

Considering the normal stress balance at the interface represented by Eq. (12), the pressure on each side of the interface needs to be obtained. This is achieved if one defines a system of coordinates at the interface, such that η and ξ are coordinates oriented along the tangential and normal directions to the interface. Now, the pressure in each phase at the interface may be obtained by solving the momentum equation at the interface, which may be written in the form (Ryskin and Leal [36])

$$\nabla(p + \varrho \mathbf{uu}) = (\varrho \mathbf{u} \times \mathbf{w}) - 2\nabla \times \mathbf{w}, \tag{60}$$

where ω is the vorticity. Integrating this expression along the η-direction and considering the idealized case of inviscid, irrotational flow, one obtains

$$p_{i/o} = (p_c)_{i/o} - \varrho_{i/o}(u_\eta^2)_{i/o}, \tag{61}$$

where the subscript i/o implies that the expression applies to both the inner and outer phases of the interface and u_η is the η (tangential)-component of the velocity at the interface. The component of pressure p_c is hydrostatic. The difference between the inner and outer hydrostatic pressure components is adjusted as described previously for enforcing mass conservation. Under this idealization, the dynamic pressure plays the dominant role in the normal stress balance at the interface. This is an important term that distinguishes the behavior of bubbles from the inviscid droplets. In the case of the bubble the dynamic contribution to pressure from the inner phase is negligible and the stability of the bubble is influenced only by the outer dynamic contribution. For the case of an inviscid droplet with the density ratio $\beta = 1$, the kinematic condition implies $(u_\eta)_i = (u_\eta)_o$. Therefore, under this condition, when the pressures at the interface as given by Eq. (61) are inserted into Eq. (12), the dynamic contributions to the normal stress balance exactly cancel. In inertia-dominated flows it is the dynamic contribution that dominates in the stress balance. Therefore, in this situation the behavior of the inviscid droplet will be vastly different from that of the bubble, where the inertia effect is negligible, and different densities of the droplet will cause different critical Weber numbers.

For the case of a droplet, since the dynamic contributions from the inner surface partially counteracts the dynamic pressure contribution on the outer phase, the critical Weber number may be expected to be higher than that for a bubble. In the simulations presented here, the ratios of density and viscosity are $\beta = 0.02$ and $\lambda = 0.02$. To see what the flowfield characteristics are in this case, we plot in Fig. 17a the velocity vectors for a We $= 1.2$, i.e., the critical value. In 17b the pressure contours and in 17c the pressure profiles are shown at eight equally-spaced sections along the x-axis in the region occupied by the droplet. The arrow shows the direction of increasing i. As seen in Figs. 17b and c, there is a jump in the pressure at the interface location. It is seen from this figure that, although the pressure at each x-station inside the droplet is practically constant, there is a variation of the pressure in the droplet in the tangential direction. In fact, the pressure rises somewhat as one goes from the top of the droplet toward the side. Although this rise in pressure is not as high as that on the outer phase as can be clearly seen in Fig. 17c, this may lead to the enhanced stability in the present case when compared to a bubble, where the pressure inside is a contant and is solely hydrostatic. Note that in the interior of the droplet the pressure along the interface rises from the value of about 1.7 to 1.95 ($\delta p = 0.25$), while outside the droplet it decreases from -0.8 to about -2.3 ($\delta p = -1.5$). Therefore, the tangential increment of the pressure inside the droplet is nonnegligible compared to that outside. In Fig. 17d we present the u-velocity profiles at the same sections as the p-profiles in 17c. As can be seen large velocity gradients exist in the interior of the droplet due to the strongly recirculating flow present there. However, the viscous stresses in the droplet, in relation to that outside, may not significantly influence the droplet stability via Eq. (12) in view of

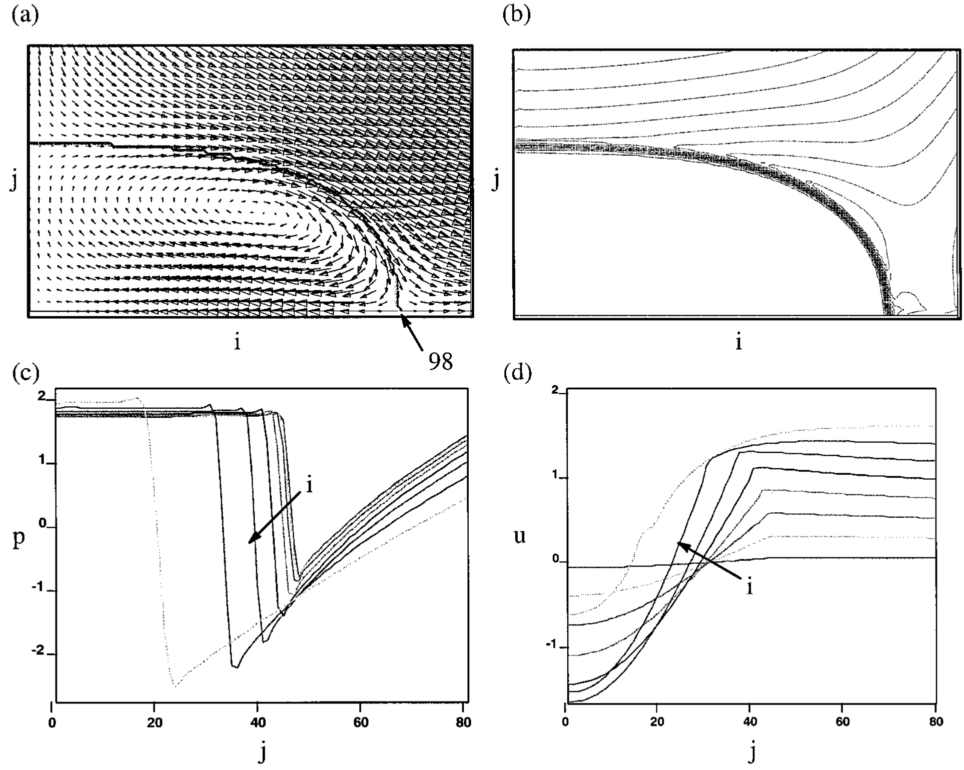

FIG. 17. Flowfield characteristics for the case of droplet in extensional flow at Re = 10, We = 1.2, $\beta = 0.02$, $\lambda = 0.02$. (a) Velocity vectors in the region containing the droplet. (b) Pressure contours in the same region. (c) Pressure profiles at eight different sections along the x-axis starting from $i = 4$ to $i = 95$ (droplet extends from $i = 1$ to $i = 98$). Arrow indicates increasing i. (d) u-velocity profiles at the same stations as in (c).

the inertia-dominated flow and due to the viscosity inside the droplet being 0.02 times the outer viscosity. It is not straightforward to quantify the individual contributions of the viscous stresses and the pressure terms in the balance expression given by Eq. (12) due to the nonlinearity of the flowfield. At the present time, based on the flow quantities displayed in these figures, it is proposed that the discrepancy in the $\mathrm{We}_{\mathrm{cr}}$ value is due to the fact that even for the fairly large density and viscosity jumps considered here, the dynamics internal to the droplet is nonnegligible. Further investigation of these aspects is required and is in progress. Suffice it to say that, as pointed out by Ryskin and Leal [36], the results from studies of the behavior of bubbles do not carry over directly to inviscid droplets, except at negligible Reynolds numbers; for the imposed flow at small Reynolds numbers, the pressure inside the bubble and inviscid droplet are constant, since the dynamic contribution to pressure does not exist.

3.2.3. *Deformation of Droplets in Constricted Tubes*

In the above sections we have demonstrated the ability of the algorithm to (1) handle complex flows in the arbitrary domains represented on a Cartesian grid, (2)

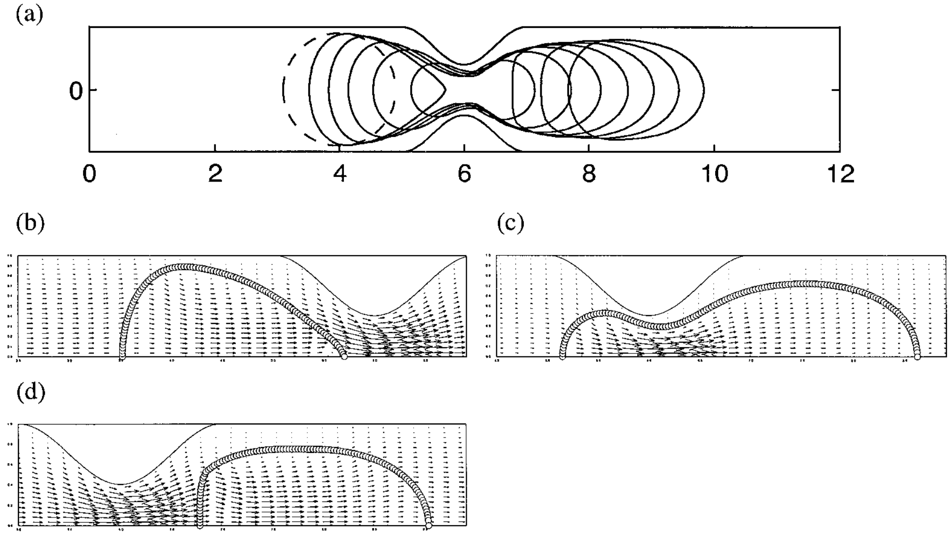

FIG. 18. Flow of a droplet through a constricted tube for the case of Re = 0.0, Ca = 0.1, $\beta = 1$, $\lambda = 0.01$, $a = 0.9$. (a) The interface shapes shown at nondimensional times of 0.0, 0.25, 0.5, 0.75, 1.0, 1.25, 1.5, 1.75, 2.0. (b), (c), and (d) Velocity vectors for the times 0.25, 1.25, and 1.5, respectively.

to accurately obtain the dynamics of interfaces under the balance of inertia, viscous, and capillary forces. In this section we tie these aspects together in studying the deformation of droplets in viscosity and inertia dominated flows through a constricted tube. The interaction of droplets with the geometry in which they are constrained to traverse has received some attention from experimental (Olbricht and Kung [37], Olbricht and Leal [38]) and numerical viewpoints (Tsai and Miksis [39], Manga [40, 41]). Since the major focus has been on the behavior of multiphase flow through porous media with applications in oil recovery, such flows have been restricted to the creeping flow regime. The boundary integral technique was applied to simulate such a problem by Tsai and Miksis [39]. In recent work, Manga [40, 41] applied the same technique to study the behavior of droplets in geometries such as a driven cavity and bifurcating channel, again restricted to Stokes flow. To our knowledge, numerical work on the behavior of droplets in fixed geometries with significant inertia effects has been restricted to the study of droplets in straight capillaries (Lee *et al.* [42]). While the boundary integral technique is unable to handle flows with convection, purely Eulerian methods have to contend with limitations imposed by the Cartesian grid on which they are based. The present algorithm does not suffer from these limitations and thus will be employed below to investigate the flow of droplets in a constricted tube at nonvanishing Reynolds numbers.

In Fig. 18, we show the results of the simulation of droplet motion through a constricted tube at small Reynolds number. For this case, we have employed the same conditions as one of the cases in Tsai and Miksis [39]. The constriction in the tube is a sine wave with amplitude 0.6 R and wavelength 2.0 units, where R is the radius of the tube. For this case Ca = 0.1, the density ratio $\beta = \varrho_i/\varrho_o = 1$, the viscosity ratio $\lambda = \mu_i/\mu_o = 0.01$ and the ratio of the undeformed droplet radius to

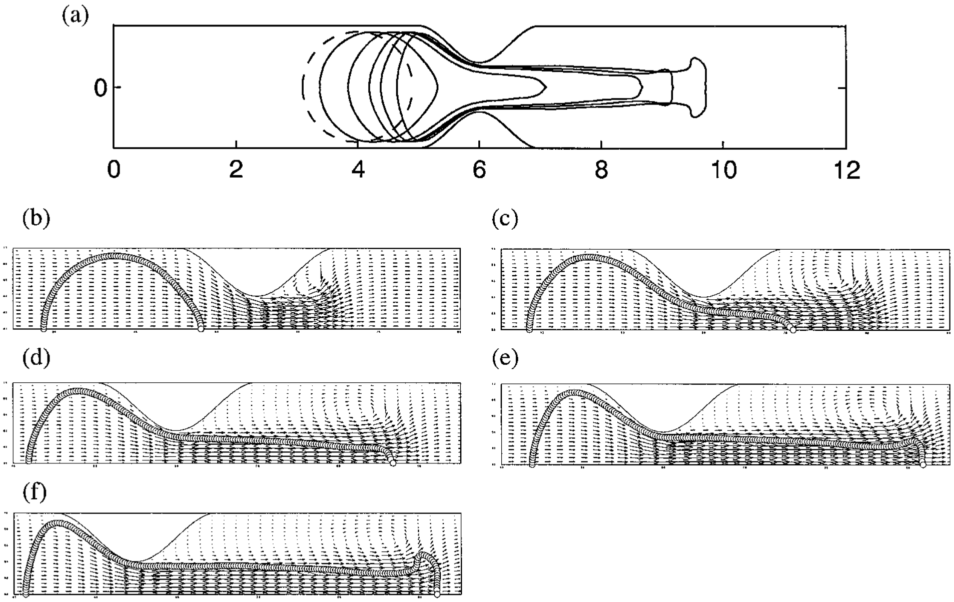

FIG. 19. Entry of a droplet into a constricted tube for Re = 50, Ca = 0.1, $\beta = 1$, $\lambda = 0.01$, a = 0.9. (a) droplet shapes at t = 0, 0.25, 0.625, 0.875, 1.0, and 1.12. (b)–(f) Velocity vectors at t = 0.25, 0.625, 0.875, 1.0, and 1.12, respectively.

the tube radius, $a = 0.9$. As in the case of Tsai and Miksis [39], the circular droplet is placed initially such that its center is at $x = 4.0$. The initial shape of the droplet is shown by the dotted lines in Fig. 18a. The evolution of the droplet is shown at equal intervals ($\delta t = 0.25$) of time. The interface shapes at these instants agree remarkably well with the results of Tsai and Miksis [39] using the boundary integral technique. As can be seen, the droplet deforms essentially in conformity with the shape of the constriction for this case. In Figs. 18b to d we show the velocity vectors for this case at instants before, during, and after passage of the droplet through the constriction. The effect of capillarity can be seen in these figures from the turning of the velocity vectors in the region where the flowfield is not strong, such as at the regions close to the wall. Also to be noticed is that at the entry to the constriction the front of the bubble is sharpened and at the exit the rear is flattened by the acceleration of the flow at the constriction. This example serves to illustrate a fairly simple configuration that can be handled by the present algorithm for interaction of multiphase dynamics through complex geometry.

As an additional element in the physics we simulate the flow of the same droplet in the constricted tube, but under convective flow conditions. In this regime the boundary integral technique used by Tsai and Miksis [39] cannot be applied due to the nonlinear field equations. The Reynolds number based on the tube radius is 50. For the case shown in Fig. 19, Ca = 0.1, $\beta = 1$, $\lambda = 0.01$, and $a = 0.9$. The response of the droplet in this situation is significantly different. Due to the presence of the recirculation zone aft of the constriction the picture changes drastically. For the area ratio and Reynolds number considered, there appears to be an unsteady

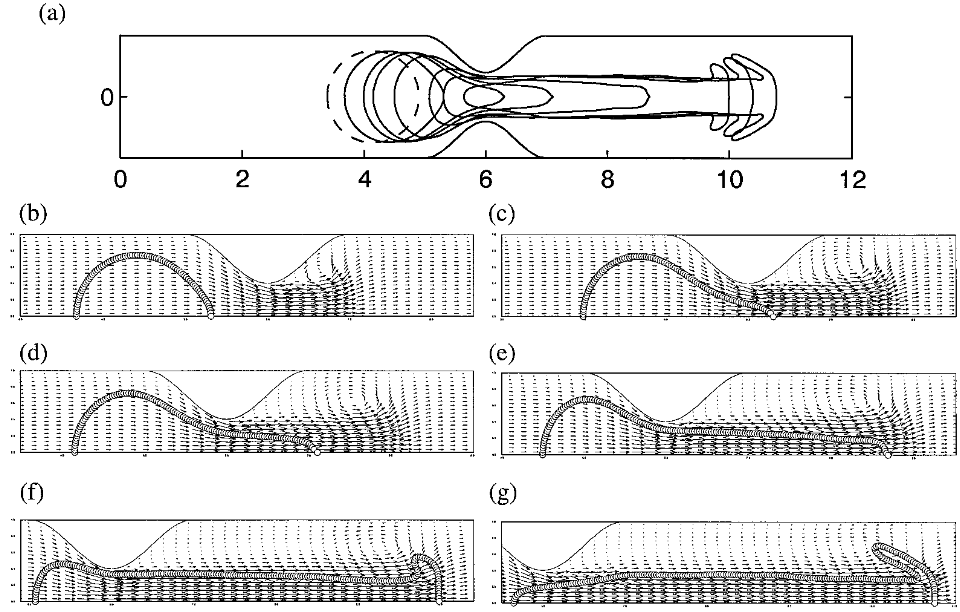

FIG. 20. Entry of a droplet into a constricted tube for Re = 50, Ca = 0.1, β = 1, λ = 0.01, a = 0.75. (a) Shapes of the droplet t = 0.0, 0.25, 0.5, 0.625, 0.875, 1.25, 1.375, 1.5. (b)–(g) Velocity vectors at t = 0.25, 0.5, 0.625, 0.875, 1.25, 1.5, respectively.

motion in the region following the constriction. A region of recirculating flow is formed and travels downstream of the throat. This region of the flow has a profound effect on the interface shape. The interface gets stretched into an elongated shape downstream of the constriction due to the higher flow speeds there on account of the rapid area change. Since the material boundary is convected with the flow, the elongated droplet shape is formed. As the droplet develops, however, the shedding recirculating flow region has an effect on the interface and draws the front end of the interface into the shape seen in the Fig. 19a. In this case, as the interface deforms, the rear of the droplet is pushed toward the constriction and flattened. Ultimately, the droplet collides with the wall, at which point we terminate the calculations due to uncertainty in the subsequent behavior. One possibility is that the droplet will eventually pass through the constriction, as the film of liquid squeezed between the droplet and the wall of the tube may act as a lubricating layer, facilitating the motion of the interface relative to the wall. This behavior cannot be captured due to the finite resolution afforded by the grid. Alternatively, the collision with the wall may result in rupture of the droplet surface leading to breakup. Since the impending events are somewhat nebulous, we present results only up to the stage that the collision is detected by the algorithm.

As a contrasting case, we perform the same simulation for a smaller droplet, for which a = 0.75. All other conditions are identical to the previous case. From Fig. 20, it is seen that the dynamics is very similar to the case of the larger droplet, except that eventually the droplet passes through the constriction. Since the calculation was carried further than in the previous case, it is seen that the translating recirculating flow structure downstream of the constriction continues to deform the droplet there, resulting in the flattened structure of the fore end of the droplet. For the given Ca = 0.1, the inertia effects appear to dominate over the capillary forces as there is hardly any difference in the behavior of the smaller droplet in comparison to the larger droplet. Due to the larger surface curvatures of the smaller droplet, in the case of sufficiently small capillary numbers, it is expected that the droplet size will have an effect on its interaction with the flowfield. Also, due to the unsteady nature of the flowfield, the precise shape of the droplet downstream of the throat will depend on the relative phase of shedding in that region and droplet entry aft of the throat. Also, from preliminary studies for a lower Reynolds number, where shedding is absent, the behavior of the droplet is noticed to be significantly different from that presented here. The facility developed here is being applied to investigate these issues.

In this work, we have mainly focussed on the numerical aspects of the algorithm and have elucidated the physics only from the viewpoint of establishing the physical correctness of the results obtained. In a related work, we have applied the technique developed here to study the dynamics of encapsulated viscous droplets as a model for leukocyte dynamics (Kan [43]).

4. CONCLUSIONS

In this paper we have described three types of extensions to the algorithm called *ELAFINT*, which may be summarized as follows:

1. A collocated variable approach is adopted. The stability and accuracy of the algorithm in computing flows of comparable complexity to those handled by the staggered grid approach was established. The collocated layout considerably simplifies the algorithm.

2. The cut-cell technique is facilitated by the collocated grid layout and is rendered less tedious. While previously the cut-cell technique had to contend with three types of control volumes, in the present case only one control volume is used.

3. The fluid–fluid interface has been modeled using the immersed boundary technique. The cut-cell approach was used in previous work on solidification for the moving boundary calculations. For the fluid–fluid interfaces, however, the method proved to be sensitive to noise and was difficult to stabilize. This is because the cut-cell method employs no dissipation, so that the boundary condition application is exact. In other moving boundary treatments based on a fixed grid, some smearing is added near the discontinuity. This is the case in the immersed boundary technique (Unverdi and Tryggvason [9]), the VOF method (Kothe *et al.* [5]) and the level-set method (Sussman *et al.* [6], Sethian [8], Chang *et al.* [44], Hou *et al.* [45]). The choice of the immersed boundary technique was made due to its compatibility with explicit interface tracking where ambiguity in regard to interface location is avoided.

The performance of the method under the above modifications has been demonstrated. The applications include:

(1) Flows in complex two-dimensional geometries under significant convection, which obviates the need for grid-generation. In this part we have compared results, where possible, to a boundary-fitted code and shown good comparison.

(2) The results of the deformation and recovery of viscous drops, subjected to a uniaxial extensional flow, show good agreement with those of Stone and Leal [31, 34]. Thus, it is established that the viscous–capillary balance is well captured by the numerical technique.

(3) The deformation of droplets under uniaxial extension flow under convective conditions has been studied. In contrast with the work by Kang and Leal [2], here we consider the motion of the fluid inside the droplet. It is interesting to note that the estimated critical Weber number for the present simulation is somewhat higher than that predicted by Ryskin and Leal [36] for a bubble with no internal dynamics. As discussed in Reskin and Leal [36], this discrepancy in predicting critical Weber numbers is expected. In line with Mashayek and Ashgriz [35], the relaxation oscillations of the drop under the competition between inertia and capillary forces is observed.

(4) Finally, the various aspects of the algorithm tested above are grouped together in order to study the behavior of drops in constricted tubes. For low Reynolds number flows, we show that the results of Tsai and Miksis [39] are reproduced. But we go beyond this creeping flow regime, and find some interesting behaviors of the drop in the region downstream of the throat at Re = 50.

Thus, the algorithm presented above has some attractive features in comparison to existing methods for moving boundary problems. The algorithm is being applied to study other problems involving interaction of multiphase flows with flow geometries.

ACKNOWLEDGMENT

The authors acknowledge the support provided by the National Institute of Health, through Grant 4-RO1-HL-49060 and by the U.S. Air Force for this research. We thank one of the reviewers for an extremely thorough reading of the original version of this paper. The suggestions made by the reviewer have substantially helped us improve the presentation of the work.

REFERENCES

1. W. Shyy, H. S. Udaykumar, M. M. Rao, and R. W. Smith, *Computational Fluid Dynamics with Moving Boundaries* (Hemisphere, Washington, DC, 1996).
2. I. S. Kang and L. G. Leal, Numerical solution of axisymmetric, unsteady free-boundary problems at finite Reynolds number. I. Finite-difference scheme and its application to the deformation of a bubble in a uniaxial straining flow, *Phys. Fluids* **30**(7), 1929 (1987).
3. J. Glimm, J. Grove, B. Lindquist, O. A. McBryan, and G. Tryggvason, The bifurcation of tracked scalar waves, *SIAM J. Sci. Stat. Comput.* **9**(1), 61 (1988).
4. S. Osher and J. A. Sethian, Fronts propagating with curvature dependent speed: Algorithms based in Hamilton–Jacobi formulations, *J. Comput. Phys.* **79,** 12 (1988).
5. D. B. Kothe and R. C. Mjolsness, RIPPLE: A new method for incompressible flows with free surfaces, *AIAA J.* **30**(11), 2694 (1992).

6. M. Sussman, P. Smereka, and S. Osher, A level set approach for computing solutions to incompressible two-phase flow, *J. Comput. Phys.* **114,** 146 (1994).
7. C. W. Hirt and B. D. Nichols, Volume of fluid (VOF) method for the dynamics of free boundaries, *J. Comput. Phys.* **39,** 201 (1981).
8. J. A. Sethian, *Level Set Methods: Evolving Interfaces in Geometry, Fluid Mechanics, Computer Vision, and Materials Science* (Cambridge Univ. Press, Cambridge, 1996).
9. S. O. Unverdi and G. Tryggvason, A front tracking method for viscous, incompressible, multifluid flows, *J. Comput. Phys.* **100,** 25 (1992).
10. M. R. Nobari, Y.-J. Jan, and G. Tryggvason, Head-on collision of droplets—A numerical investigation, *Phys. Fluids* **8**(1), 29 (1996).
11. H. S. Udaykumar and W. Shyy, Simulation of morphological instabilities during solidification; part I: conduction and capillarity effects, *Int. J. Heat Mass Transf.* **38,** 2057 (1995).
12. H. S. Udaykumar, M. M. Rao, and W. Shyy, *ELAFINT*—A mixed Eulerian–Lagrangian method for fluid flows with complex and moving boundaries, *Int. J. Numer. Meths. Fluids.* **22**(8), 691 (1996).
13. D. Juric and G. Tryggvason, A front tracking method for dendritic solidification, *J. Comput. Phys.* **123,** 127 (1996).
14. J. J. Quirk, *An Alternative to Unstructured Grids for Computing Gas Dynamic Flows around Arbitrarily Complex Two-Dimensional Bodies, ICASE Report No. 92-7,* NASA Langley Research Center, Hampton, VA, 1992.
15. R. B. Pember, J. B. Bell, and P. Colella, An adaptive Cartesian grid method for unsteady compressible flow in irregular regions, *J. Comput. Phys.* **120,** 278 (1995).
16. D. P. Young, R. G. Melvin, M. B. Bieterman, F. T. Johnson, S. S. Samant, and J. E. Bussoletti, A locally refined rectangular grid finite element method: Application to computational fluid dynamics and computational physics, *J. Comput. Phys.* **92,** 1 (1992).
17. D. D. Zeeuw and K. G. Powell, *An Adaptively-Refined Cartesian Mesh Solver for the Euler Equations, AIAA Paper No. 90-0000* (1990).
18. S. A. Bayyuk, K. G. Powell, and B. van Leer, *A Simulation Technique for 2-D Unsteady Inviscid Flows around Arbitrarily Moving and Deforming Bodies of Arbitrary Geometry, AIAA Paper No. 93-3391* (1993).
19. D. Goldstein, R. Handler, and L. Sirovich, Modeling a no-slip surface with an external force field, *J. Comput. Phys.* **105,** 354 (1993).
20. D. Goldstein, R. Handler, and L. Sirovich, Direct numerical simulation of turbulent flow over a modeled riblet covered surface, *J. Fluid Mech.* **302,** 333 (1995).
21. C. S. Peskin, Numerical analysis of blood flow in the heart, *J. Comput. Phys.* **25,** 220 (1977).
22. H. Miyata, Finite difference simulation of breaking waves, *J. Comput. Phys.* **65,** 179 (1986).
23. H. S. Udaykumar and W. Shyy, A grid-supported marker particle scheme for interface tracking, *Num. Heat Transf. B* **27**(2), 127 (1995).
24. F. S. Lien and M. A. Leschziner, A general non-orthogonal collocated finite volume algorithm for turbulent flow at all speeds incorporating second-moment turbulence-transport closure, parts 1 & 2: computational implementation and applications, *Comput. Methods Appl. Mech. Engrg.* **114,** 123 (1994).
25. S. V. Patankar, *Numerical Heat Transfer and Fluid Flow* (Hemisphere, Washington, DC, 1980).
26. W. Shyy, *Computational Modelling for Fluid Flow and Interfacial Transport* (Elsevier, Amsterdam, 1994).
27. L. J. Fauci and C. S. Peskin, A computational model of aquatic animal locomotion, *J. Comput. Phys.* **77,** 85 (1988).
28. C. M. Rhie and W. L. Chow, Numerical study of turbulent flow past an airfoil with trailing edge separation, *AIAA J.* **21,** 1525 (1983).
29. S. Majumdar, Role of underrelaxation in momentum interpolation for calculation of flow with nonstaggered grids, *Numer. Heat Transfer* **13,** 125 (1988).

30. C. S. Peskin and B. F. Printz, Improved volume conservation in the computation of flows with immersed elastic boundaries, *J. Comput. Phys.* **105,** 33 (1993).
31. H. A. Stone and L. G. Leal, Relaxation and breakup of an initially extended droplet in an otherwise quiescent fluid, *J. Fluid Mech.* **198,** 399 (1989).
32. W. Shyy and M. M. Rao, Calculation of meniscus shapes and transport processes in float zone, *Int. J. Heat Mass Transf.* **38,** 2281 (1995).
33. S. Thakur, J. Wright, W. Shyy, J. Liu, H. Ouyang, and T. Vu, Development of pressure-based composite multigrid methods for complex fluid flows, *Prog. Aerosp. Sci.* **32,** 313 (1996).
34. H. A. Stone and L. G. Leal, The influence of initial deformation on droplet breakup in subcritical time-dependent flows at low Reynolds numbers, *J. Fluid Mech.* **206,** 223 (1989).
35. F. Mashayek and N. Ashgriz, A spline-flux method for simulating free surface flows, *J. Comput. Phys.* **122,** 367 (1996).
36. G. Ryskin and L. G. Leal, Numerical solution of free-boundary problems in fluid mechanics. Parts I, II, and III, *J. Fluid Mech.* **148,** 1 (1984).
37. W. L. Olbricht and D. M. Kung, The deformation and breakup of liquid droplets in low Reynolds number flow through a capillary, *Phys. Fluids* **4**(7), 1347 (1992).
38. W. L. Olbricht and L. G. Leal, The creeping motion of immiscible droplets through a converging/diverging nozzle, *J. Fluid Mech.* **134,** 329 (1993).
39. T. M. Tsai and M. J. Miksis, Dynamics of a droplet in a constricted capillary tube, *J. Fluid Mech.* **274,** 197 (1994).
40. M. Manga, Dynamics of droplets in cavity flows: Aggregation of high viscosity ratio droplets, *Phys. Fluids* **8**(7), 1732 (1996).
41. M. Manga, Dynamics of droplets in branched tubes, *J. Fluid Mech.* **315,** 105 (1996).
42. Y. L. Lee, R. L. Panton, and K. S. Ball, Steady shape of a bubble in flow through a vertical capillary tube, *Proceedings of the ASME Fluids Engineering Division,* FED, Vol. 234, IMECE, 1995.
43. H.-C. Kan, *Computational Study of Leukocyte Rheology Based on A Multilayer Fluid Model,* Ph.D. thesis, The University of Florida, 1997.
44. Y. C. Chang, T. Y. Hou, B. Merriman, and S. Osher, A level set formulation of Eulerian capturing methods for incompressible fluid flows, *J. Comput. Phys.* **124,** 449 (1996).
45. T. Y. Hou, Z. Li, S. Osher, and H. Zhao, A hybrid method for moving interface problems with applications to the Hele–Shaw flow, *J. Comput. Phys.* **134,** 236 (1997).